THE UNIVERSITY OF TULSA

THE GRADUATE SCHOOL

HYBRID MULTICONTINUUM AND DISCRETE FRACTURE-MATRIX DISCRETIZATION SCHEMES FOR UNCONVENTIONAL RESERVOIR SIMULATION

by
Jiamin Jiang

A thesis submitted in partial fulfillment of

the requirements for the degree of Master of Science

in the Discipline of Petroleum Engineering

The Graduate School

The University of Tulsa

2015

THE UNIVERSITY OF TULSA

THE GRADUATE SCHOOL

HYBRID MULTICONTINUUM AND DISCRETE FRACTURE-MATRIX DISCRETIZATION SCHEMES FOR UNCONVENTIONAL RESERVOIR SIMULATION

by
Jiamin Jiang

A THESIS

APPROVED FOR THE DISCIPLINE OF

PETROLEUM ENGINEERING

By Thesis Committee

______________________________, Chair
Rami Younis

____
Leslie Thompson

____
Randy Hazlett

____
Mohammad Shahvali

COPYRIGHT STATEMENT

ABSTRACT

Jiamin Jiang (Master of Science in Petroleum Engineering),

Hybrid Multicontinuum and Discrete Fracture-Matrix Discretization Schemes for Unconventional Reservoir Simulation

Directed by Rami Younis

96, pp., Chapter 4: Conclusions

(408 words)

Unconventional reservoirs are the focus of considerable attention as a primary energy source. Numerical simulation is a core kernel of reservoir engineering workflows for reservoir evaluation, optimization, and management. Accurate and efficient numerical simulation of unconventional reservoirs is challenging. There is substantial physical complexity involving a number of tightly coupled mechanisms in the modeling of these reservoirs. The complexity is further amplified by the multicontinuum nature of the stimulated formation, and the complex fracture networks with a wide range of fracture length scales and topologies.

In this work, we develop a generic simulation platform which allows investigators to rapidly implement and experiment with a wide array of alternate physical and constitutive models. In order to adequately capture the effects of the multi-scaled fracture system, we develop two alternate hybrid approaches that are aimed at combining the advantages of multicontinuum and discrete fracture-matrix (DFM) representations. During the development of unconventional resources, geological and geophysical information may be available in some cases to suggest a prior characterization, but in many other cases, this prior model may be incomplete and limited to hydraulic fractures. The two hybrid approaches could be utilized for different applications depending on the available characterization data and the different requirements for efficiency and accuracy considerations.

The first hybrid model couples EDFM with MINC (EDFM-MINC) in order to simulate the fracture network characterized by stimulated reservoir volume (SRV) concept. This optimized model could reduce the computational cost that is associated with the widely applied logarithmically spaced, locally refined (LS-LR) DFM technique, while improving the flexibility to model the complex geometry of hydraulic fractures. The MINC concept allows the hybrid model to handle the extreme contrast in conductivity between the small-scale fracture network and the ultra-tight matrix that results in steep potential gradients.

For the second class of hybrid model (UDFM-MINC), the primary fractures are described using DFM with unstructured gridding, and the small-scale fractures are simulated by continuum-type approaches in a fully coupled manner. Optimized local grid refinement (LGR) is employed to accurately handle the transient flow regime around primary fractures. An upscaling technique that applies EDFM on the detailed realization of the DFN using the target unstructured grid in order to generate an appropriate dual-permeability (DK) model is also developed. The upscaling technique is suitable for cases where a detailed prior model for the complete fracture network is available.

Simulation studies demonstrate the applicability of the developed simulation platform. Model verification is conducted against several reference solutions.

ACKNOWLEDGEMENTS

First and foremost, I would like to express my sincere thanks to my adviser, Dr. Rami Younis, who has guided me through the years. During my study at TU, I have benefited tremendously from his thoughtful guidance and insightful suggestions. Dr. Younis has been a consistent source of knowledge, advice and encouragement, not only to my research work, but also to my personal life.

I would also like to thank other members of my dissertation committee, Dr. Leslie Thompson, Dr. Randy Hazlett, and Dr. Mohammad Shahvali, for their time and effort to serve on my committee and review my dissertation. Dr. Thompson has helped me with many things, from research ideas to paper writing and valuable comments. For this, I owe him many thanks.

I owe my gratitude to the Department of Petroleum Engineering, all the faculty, staff, and my fellow students. They made my years at TU inspiring and rewarding. Their great help and friendship are very much appreciated.

I would like to express my deepest gratitude to my parents for their endless love, support, and encouragement throughout my graduate study at TU. My achievements would not have been possible without their help and inspiration.

TABLE OF CONTENTS

COPYRIGHT STATEMENT iii

ABSTRACT iv

ACKNOWLEDGEMENTS vi

TABLE OF CONTENTS vii

LIST OF FIGURES ix

INTRODUCTION 1

CHAPTER 1: **REVIEW OF MULTICONTINUUM AND DFM BUILDING BLOCKS** 6
- 1.1 **Dual-Continuum Models** 6
  - 1.1.1 *Shape Factor* 8
  - 1.1.2 *Multicontinuum Modeling with the MINC Concept* 9
- 1.2 **Discrete Fracture Models** 13
  - 1.2.1 *EDFM* 13
  - 1.2.2 *Unstructured DFM* 16

CHAPTER 2: **HYBRID COUPLED DISCRETE FRACTURE-MATRIX AND MULTICONTINUUM MODELS** 20
- 2.1 **Physical Model** 22
  - 2.1.1 *Apparent Permeability* 22
  - 2.1.2 *Governing Equations* 23
  - 2.1.3 *Finite-Volume Discretization* 25
- 2.2 **Proposed Hybrid Models and an Associated Upscaling Process** 27
  - 2.2.1 *Hybrid Model I: EDFM-MINC* 27
  - 2.2.2 *Hybrid Model II: UDFM-MINC* 29
  - 2.2.3 *Unstructured Dual-Permeability (DK) Upscaling Method* 30
- 2.3 **Model Validation** 34
  - 2.3.1 *Problem 1: Linear Gas Flow of Fractured Well at Constant BHP* 34
  - 2.3.2 *Problem 2: Two-Dimensional Transient Flow with Multiple Hydraulic Fractures* 37
  - 2.3.3 *Problem 3: Hybrid Fracture Model I (EDFM-MINC)* 38
  - 2.3.4 *Problem 4: Hybrid Fracture Model II (Unstructured DFM)* 41

2.4 **Further Simulation Examples**........ 45
  2.4.1 *Hybrid Model I: EDFM-MINC*........ 45
    2.4.1.1 Effect of MINC Refinement and Fracture Network Spacing: 46
    2.4.1.2 Effect of Two-Well Interference: 47
  2.4.2 *Hybrid Model II: UDFM-MINC*........ 49
    2.4.2.1 Grid Sensitivity: 49
    2.4.2.2 Effect of Storage and Transport Mechanism: 51
    2.4.2.3 Uncertainty Analysis of Multiple Realizations for Natural Fracture Network: 52

CHAPTER 3: **RATE TRANSIENT EFFECTS OF VARIOUS COMPLEX FRACTURE NETWORK TOPOLOGIES**........ 55
3.1 **Numerical Model and Simulation Approach**........ 56
  3.1.1 *Unstructured Gridding for Complex Fracture Network*........ 56
  3.1.2 *Mimetic Finite Difference Method*........ 57
  3.1.3 *Lower-Dimensional DFM Discretization*........ 61
3.2 **Simulation Results and Discussions**........ 63
  3.2.1 *Effect of Storage and Transport Mechanisms*........ 64
  3.2.2 *Comparison Between TPFA and MFD Scheme*........ 67
  3.2.3 *Effect of Non-Orthogonal Fracture Geometry*........ 69
  3.2.4 *Effect of Non-Planar Fracture Geometry*........ 71
  3.2.5 *Effect of Inclined Fracture Geometry*........ 74
  3.2.6 *Effect of the Stimulated Fracture Network with Secondary Fractures*........ 75
  3.2.7 *Effects on the Interpretation of Rate Transient Data*........ 79

CHAPTER 4: **CONCLUSIONS**........ 83

LIST OF FIGURES

1.1 An idealized sugar cube representation of a fractured reservoir (Warren and Root 1963). 7

1.2 MINC concept of the multicontinuum model. 10

1.3 Schematic comparing the LS-LR method with the MINC model 12

1.4 Coupled flow of MINC model with organic-inorganic-fracture configuration 13

2.1 Schematic for computing the two-point transmissibility 26

2.2 Example of the connection list for EDFM coupled with MINC 29

2.3 Grid domain and computational domain for the hybrid model 30

2.4 Schematic of unstructured gridding and embedded fracture network in the hybrid model 31

2.5 Schematic for the f-f, F-f connections 33

2.6 Schematic for an embedded fracture intersecting with matrix gridblock 34

2.7 Gas rate of the semi-analytical and numerical solution (with 161, 4001 number of gridblocks) 36

2.8 Relative error versus number of gridblocks 36

2.9 Comparison result for pressure and pressure derivative between semi-analytical and numerical solution 37

2.10 Comparison result for the gas rates of 10m fracture spacing 39

2.11 Comparison result for the gas rates of 30m fracture spacing 40

2.12 Comparison result for the gas rates of 60m fracture spacing 40

2.13 Schematics for the hybrid (9916) and reference (fine-scale) model 43

2.14 Pressure profile of the matrix at 600day for the hybrid (9916) and reference model 43

2.15 Pressure profile of the matrix at 1200day for the hybrid (9916) and reference model 43

2.16 Gas rates for the first 100 and 1200 days obtained from the hybrid and reference model 44

2.17 Schematic of the two-well interference model 46

2.18 Gas rates of Well 2 for different combinations of fracture network spacing and MINC refinement 47

2.19 Cumulative gas production for the two-well case 48

2.20 Pressure profile of the fracture continuum at 500/1000 day 49

2.21 Mesh configuration and pressure profile of the fracture continuum at 2200 day of the three cases 51

2.22 Log-Log plot for the gas rates of the three cases 51

2.23 Effect of storage and transport mechanisms on gas rate/cumulative production 52

2.24 Stochastically generated DFN and pressure profile of the matrix at 2200 day of the three cases 53

2.25 Cumulative gas production for the three cases and the base case 54

3.1 Schematic for two neighboring gridcells 59

3.2 Schematic of FCFE concept for treating fracture-matrix interface (modified from Hoteit and Firoozabadi 2008) 61

3.3 Schematic for fracture intersection 62

3.4 Mesh configuration and pressure profile at 2500 day of the “AllMechs” case 65

3.5 Effect of storage and transport mechanisms on gas rate 66

3.6 Pressure profile at 2500 day of TPFA and MFD for the diagonal permeability 68

3.7 Pressure profile at 2500 day of TPFA and MFD for the full-tensor permeability 68

3.8 Log-Log plot for the gas rates of the case with isotropic permeability 68

3.9 Log-Log plot for the gas rates of the case with diagonal permeability 69

3.10 Log-Log plot for the gas rates of the case with full-tensor permeability 69

3.11 Log-Log plot for the gas rates of the four cases 70

3.12 Mesh configuration and pressure profile at 2000 day of the three cases with non-orthogonal fracture geometry 71

3.13 Fracture geometry induced by the effect of stress shadowing for two cases with different fracture spacing 72

3.14 Mesh configuration and pressure profile at 2500 day of the two cases with non-planar fracture geometry 73

3.15 Log-Log plot for the gas rates of the three cases 73

3.16 Mesh configuration of the model that contains 3 hydraulic fractures 75

3.17 Log-Log plot for the gas rates of the four cases 75

3.18 Mesh configuration of the regular and complex cases 76

3.19 Pressure profile at 50/200 day for the complex case with the secondary fracture network 76

3.20 Log-Log plot for the gas rates of the two cases 76

3.21 The plot of inverse gas rate versus sqrt(t) for the two cases 77

3.22 Mesh configurations of the three cases 78

3.23 The plot of inverse gas rate versus sqrt(t) for the base case and the three complex cases 79

3.24 Complex fracture geometries investigated for RTA Analysis 80

3.25 Superposition Time plots 82

INTRODUCTION

Advances in formation stimulation technology are promoting global interest in the recovery of hydrocarbons from tight and shale reservoirs. In terms of unconventional reservoir management and given the underlying complexity of these systems, modeling will continue to play a critical role towards the evaluation, design, and management of stimulation and production processes (Moridis et al. 2013).

There is considerable nonlinear complexity in the modeling of unconventional reservoirs (for example, shale gas reservoirs). The gas flow is governed by a number of tightly coupled mechanisms including sorption, transport in ultra-tight porous media across various flow regimes (e.g., Knudsen, transition, slippage, and viscous effects), high-velocity turbulent flow, and rock unconsolidation within fractures (Wu et al. 2011). This complexity is further amplified by the multicontinuum nature of the stimulated formation, and the multiscale fracture networks that involve complicated geometries.

Stimulated unconventional reservoirs comprise complex fracture networks with a wide range of fracture length scales and topologies. A schematic of the types of fracture with various levels of complexity is shown in **Fig. 1** (Warpinski et al. 2008). Microseismic measurements and other geophysical evidence suggest that the creation of complex fracture networks during fracturing treatments may be a common occurrence (Weng et al. 2014). Moreover, preexisting natural fracture networks are prevalent. The stress alteration induced by hydraulic fracturing treatments may activate the preexisting natural fractures and open microscopic flow channels within the well drainage area

(Freeman et al. 2010). Secondary stress-release fractures interacting with primary fractures could have decisive influence on the well productivity, and it is very likely that their geometry is irregular with multiple orientations (Houze et al. 2010). Moridis et al. (2010) provide a classification of fracture systems that are thought to be present in stimulated unconventional gas reservoirs, and they propose that the fracture networks could contain up to four subdomains with various properties and characteristics, leading to substantial challenges in the accurate modeling of such reservoirs.

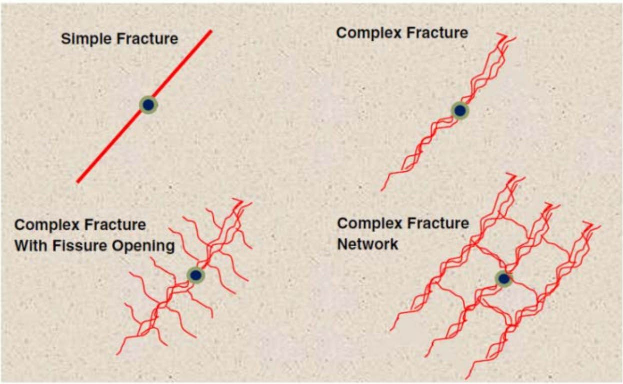

Figure 1: Schematic diagram of the types of fracture with various levels of complexity (Warpinski et al. 2008).

Broadly, two classes of numerical approaches are commonly used to model fluid flow in fractured systems, continuous representations in the form of variants of a dual-porosity/dual-permeability (DP/DK) approach and discrete representations in the forms of discrete fracture-matrix method (DFM).

The DP model proposed by Warren and Root (1963) is appropriate for reservoirs with highly connected small-scale fractures. DP models, however, are limited in their ability to represent disconnected fractured media or a small number of large-scale fractures that may dominate the flow. Moinfar et al. (2011) demonstrate examples where the DP model fails to provide satisfactory solutions in the presence of fracture systems with high heterogeneity. Moreover, the application of the traditional DP approach in unconventional reservoirs could result in large inaccuracy since it may take several years to reach the pseudo-steady state in the ultra-tight matrix systems. A multi-porosity model called multiple interacting continua (MINC) (Pruess et al. 1985; Wu et al. 1988) was proposed to simulate fully transient fracture-matrix interaction by subdividing the matrix block into strings of nested-cells. This sub-gridding strategy is a more suitable continuous numerical representation for tight and shale gas systems since it can accommodate the large potential gradients that typically arise near fractures in such reservoirs. Owing to the nonlinearity that is associated with variable gas compressibility and viscosity, the importance of this ability to resolve these gradients is even more pronounced. Farah et al. (2014) also showed that the MINC method can accurately capture water invasion near fracture faces as well as the water blocking effects due to high capillary forces in unconventional gas reservoirs. Despite advances in treatments to capture fast dynamics near fractures, continuous representations suffer from the drawback of requiring an idealized regular fracture topology that is tied to that of the underlying simulation mesh. This is a potentially serious drawback for fracture networks with disjoint, irregular, and sparse topologies.

Compared to continuous representations, DFMs attempt to incorporate explicit discretized representations of fractures and fracture segments. Subsequently, they can be used to simulate realistic, complex, and non-ideal fracture geometries, and to account for the effects of individual fractures on fluid flow explicitly. Moreover, the specification of the exchange between matrix and fracture is relatively straightforward since it depends directly on the fracture geometry. Several DFM models have been reported in the literature (for example, Kim and Deo 2000; Juanes et al. 2002; Bogdanov et al. 2003; Karimi-Fard and Firoozabadi 2003; Karimi-Fard et al. 2004; Monteagudo and Firoozabadi 2004; Matthai et al. 2005; Hoteit and Firoozabadi 2005; Reichenberger et al. 2006; Geiger et al. 2009). In addition, Lee et al. (2001), Li et al. (2008), Hajibeygi et al. (2011) and Moinfar et al. (2012) develop and improve an embedded discrete fracture model (EDFM) that incorporates the effect of each fracture explicitly without requiring the simulation mesh to conform to the fracture geometry. In EDFM, a Cartesian simulation grid may be used, and the fracture segments that intersect grid cells are treated as discrete fracture computational domains. EDFM introduces the concept of the transport index to tie the additional computational control-volumes for fractures to the matrix. Owing to the severe contrast in permeability between the matrix and fractures, DFMs typically require high levels of mesh refinement in the vicinity of fractures.

In general, the simulation of small-scale/natural fractures using DFMs is not practical due to the associated prohibitive computational cost. As a first response, hierarchical approaches have been developed where fractures at different scales are modeled differently (Lee et al. 2001). In this direction, hybrid DFM-dual-continuum approaches have been proposed where hydraulic and large-scale fractures are modeled by DFM, and a dual-continuum approach is employed to capture the dense small-scale fractures (Moinfar et al. 2013; Wu et al. 2013). **Fig. 2** illustrates the hybrid modeling approach to couple small- and large-scale fractures. In the hybrid approach, one critical aspect is to establish the link between the fine-scale discrete fracture network (DFN) and the corresponding continuum-type model. During the development of unconventional reservoirs, integrated fracture characterization data, if available, could provide multiple realizations of DFN. The fracture uniformity that is presumed by the traditional continuum-type models may not be present in these realizations. Several upscaling methods for constructing continuum-type models from DFN were developed (Dershowitz et al. 2000; Ding et al. 2006; Vitel et al. 2007; Ahmed Elfeel and Geiger 2012; Geiger et al. 2013; Maier and Geiger 2013). Karimi-Fard et al. (2006), Gong et al. (2008), Hui et al. (2013) also developed the multiple sub-region (MSR) method in order to systematically generate flow-based MINC model to resolve the matrix dynamics in each coarse block.

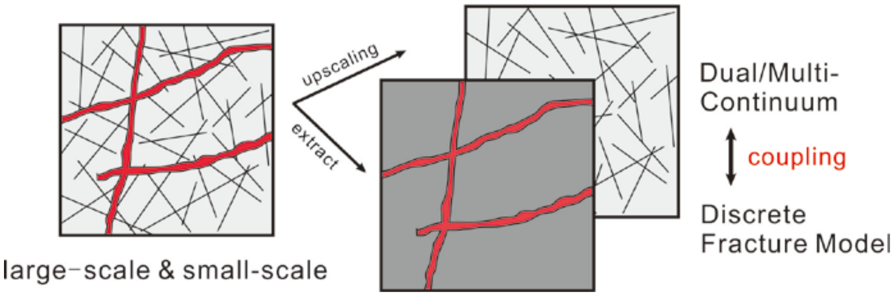

Figure 2: Schematic illustrating a hybrid modeling approach for small- and large-scale fractures.

CHAPTER 1

REVIEW OF MULTICONTINUUM AND DFM BUILDING BLOCKS

Presence of highly fracture pathways at various length scales, coupled with small fracture volumes, makes numerical simulation of fluid flow in naturally fractured reservoirs (NFRs) very challenging. Several approaches have been proposed to model NFRs, which can be categorized into two classes of models, dual continuum and discrete fracture models. Presently, dual continuum models are the most commonly used modeling approach for NFRs in the petroleum industry. However, discrete fracture modeling approaches are gaining considerable interest.

1.1 Dual-Continuum Models

Dual-continuum models, widely used in the industry, are the conventional method for simulating NFRs. Warren and Root (1963) introduced the dual porosity model to the petroleum literature. The dual porosity model, which is also known as a sugar cube model, was first used for modeling single-phase flow in NFRs. In this model, rectilinear prisms of rock matrix are separated by an orthorhombic continuum of fractures. Dual porosity simulation involves discretization of the reservoir into two domains, matrix and fracture. Hence, every point in the reservoir contains fracture and matrix pressures and saturations. A dual porosity model presumes that the flow occurs from the matrix to the fractures, and then to the production wells. The rock matrix is where the majority of oil is stored. In the dual porosity model, matrix and fracture domains are linked to each other through an exchange term that connects each fracture cell to its corresponding matrix cell in a gridblock. The matrix-fracture exchange rate is controlled by a shape factor. Also, the matrix blocks in the dual porosity approach are assumed to be isotropic and homogeneous. **Fig. 1.1** shows an idealized sugar cube representation of a fractured reservoir, wherein highly interconnected orthogonal fractures are fed by numerous matrix blocks.

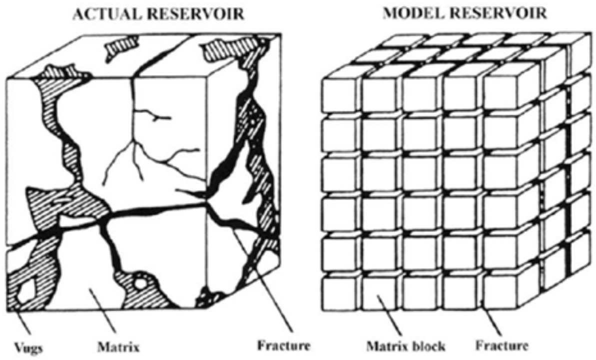

Figure 1.1: An idealized sugar cube representation of a fractured reservoir (Warren and Root 1963).

Considering single-phase fluid flow, the mass conservation equations for the fracture and matrix domains in the dual porosity approach can be expressed for the fracture domain, as

$$\frac{k_{fx}}{\mu}\frac{\partial^2 P_f}{\partial x^2}+\frac{k_{fy}}{\mu}\frac{\partial^2 P_f}{\partial y^2}+\frac{k_{fz}}{\mu}\frac{\partial^2 P_f}{\partial z^2}-q_{mf}=\phi_f C_f\frac{\partial P_f}{\partial t} \tag{1.1}$$

and for the matrix domain, as

$$\phi_m C_m\frac{\partial P_m}{\partial t}=q_{mf} \tag{1.2}$$

The matrix-fracture transfer is represented by the pseudo-steady state relation

$$q_{mf}=\frac{\sigma k_m}{\mu}\left(P_m-P_f\right) \tag{1.3}$$

where k is permeability, P is pressure, μ is fluid viscosity, C is total compressibility, ϕ is porosity, σ is shape factor, and q_{mf} is matrix-fracture flow rate per unit bulk volume. The subscripts m and f refer to the properties in the matrix and fracture domains. The shape factor, which has the dimension of reciprocal area, reflects the geometry of matrix blocks and controls the interporosity flow between matrix and fracture domains.

1.1.1 Shape Factor

The matrix-fracture exchange is a critical component of any model used for the simulation of NFRs. In the Warren and Root approach, the matrix-fracture fluid transfer is assumed to take place under pseudo-steady state conditions. As described in Eq. 1.3, the matrix-fracture transfer function is proportional to a geometrical shape factor σ, and the driving force is the pressure difference between a matrix block and its surrounding fracture. Determination of shape factor is not a simple task because of the potential for complex interaction between fractures and matrix rock of various shapes.

Originally, Warren and Root (1963) defined the shape factor as a parameter that depends on the geometry of matrix blocks, as

$$\sigma = \frac{4n(n+2)}{L^2}, \tag{1.4}$$

where n is the number of normal sets of fractures $(n = 1, 2, 3)$ and the characteristic length of matrix blocks

$$\begin{aligned} L &= a, && n = 1 \\ L &= \frac{2ab}{a+b}, && n = 2 \\ L &= \frac{3abc}{ab+ac+bc}, && n = 3 \end{aligned} \tag{1.5}$$

where a, b, and c are the lengths of the blocks faces.

Kazemi et al. (1976) used a finite-difference formulation for the flow between matrix and fractures and showed that for a three-dimensional case

$$\sigma = 4\left(\frac{1}{L_x^2} + \frac{1}{L_y^2} + \frac{1}{L_z^2}\right) \tag{1.6}$$

where L_x, L_y, and L_z are the distances between fractures in the x, y, and z directions, respectively.

These shape factors assume that the pseudo-steady state assumption is valid. Lim and Aziz (1995) considered the physics of pressure diffusion from the matrix to the fracture and presented a new shape factor as follows

$$\sigma = \pi^2\left(\frac{1}{L_x^2} + \frac{1}{L_y^2} + \frac{1}{L_z^2}\right) \tag{1.7}$$

they performed simulations to investigate the accuracy of various shape factors using fine-grid simulations. The results showed that their shape factor in Eq. 1.7 matches with the results of fine-grid single porosity better, indicating that the pseudo-steady state assumption is not a suitable one and the pressure gradients in the matrix should be taken into account for the calculation of shape factors. They also showed that the dual porosity simulation using the Warren and Root's shape factor overestimates the recovery, while the simulation using the Kazemi's shape factor underestimates the recovery.

1.1.2 Multicontinuum Modeling with the MINC Concept

Because of the ultra-low matrix permeability in unconventional formations, a long period of transient flow occurs inside the matrix (Mayerhofer et al. 2006; Warpinski et al. 2008; Cipolla et al. 2010); thus it is inaccurate to treat fracture-matrix flow as pseudo-steady state. High-resolution is needed near fractures in order to capture the large potential gradients. The MINC model treats the transient interaction between matrix and fractures in a realistic way (Pruess and Narasimhan 1985; Wu and Pruess 1988). In the MINC model, each matrix cell in the computational mesh is subdivided into a series of nested sub-cells. On the basis of the assumption that global flow occurs through the network of the well-connected micro-fractures, the reservoir could be partitioned into primary gridblocks that contain groups of elementary units for nested matrix and fracture continua. The three dimensional configuration of the MINC model comprises three orthogonal sets of natural fractures, as depicted in **Fig. 1.2**. While variables like pressure may vary strongly over small distances in the vicinity of the fractures, it is reasonable to expect that spatial variations within the fracture system may be slow and amenable to volume averaging (Pruess and Narasimhan 1985). Thus, appropriate portions of the flow region could be lumped into one computational volume element as shown in **Fig. 1.2**.

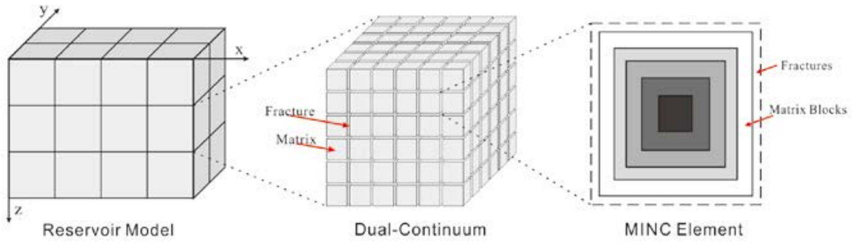

Figure 1.2: MINC concept of the multicontinuum model.

In order to describe the methodology of deriving the parameters required by the MINC concept, an idealized fractured reservoir, made up of identical rectangular blocks which are separated by fractures is considered as in Pruess and Narasimhan (1982). The interacting continua can be described through a set of elemental volumes V_i, interface areas $A_{i-1,i}$, and nodal distances $d_{i-1,i}$, which can be written as an expression of the volume fractions f_i occupied by the N interacting continua. The nested volume elements can be calculated with several approaches e.g. constant volume fractions, equidistant nested volume elements, from upscaling procedures. In a three dimensional setting, assuming that the index $i = 1$ refers to the outer fracture continuum, the volume fraction for the outer continuum in a coarse block of cubical shape having the edge L is

$$f_1 = [L^3 - (L - \delta)^3] \,/\, L^3 \approx 3\delta \,/\, L \tag{1.8}$$

where δ is the fracture aperture. The volume of continuum i in an elementary unit

$$V_i = f_i L^3, \;\; i = 1, 2, \dots, N \tag{1.9}$$

the interface area

$$A_{i,i+1} = 6L^2 \left(\sum_{j=i+1}^{N} f_j \right)^{2/3} \tag{1.10}$$

the nodal distances

$$d_{1,2} = \frac{L}{4} \left[\left(\sum_{j=2}^{N} f_j \right)^{1/3} - \left(\sum_{j=3}^{N} f_j \right)^{1/3} \right] \tag{1.11}$$

$$d_{i,i+1} = \frac{L}{4} \left[\left(\sum_{j=i}^{N} f_j \right)^{1/3} - \left(\sum_{j=i+2}^{N} f_j \right)^{1/3} \right] \tag{1.12}$$

and the interface for the innermost element V_N

$$d_{N-1,N} = \frac{L}{4} (f_{N-1} + f_N)^{1/3} - \frac{3D}{20} f_N^{\frac{1}{3}} \tag{1.13}$$

In terms of its efficacy, MINC can be compared to the logarithmically spaced, locally refined (LS-LR) DFM technique that is widely applied in commercial simulators for modeling the fracture network characterized by the SRV concept. **Fig. 1.3** illustrates how the MINC model could provide better computational efficiency relative to LS-LR while adequately capturing sharp local transients. Like MINC, LS-LR assumes an orthogonal fracture geometry; therefore, such techniques are suitable for the application scenario where detailed geological information of natural/small-scale fractures is not available.

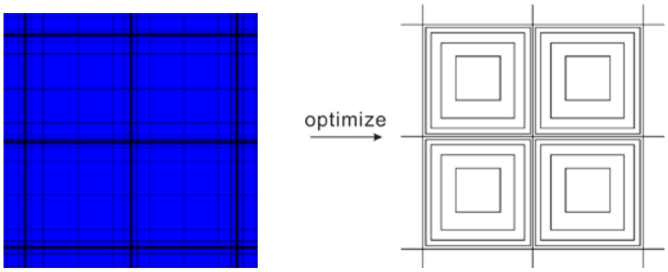

Figure 1.3: Schematic comparing the LS-LR method with the MINC model.

A preprocessing routine is developed to compute the geometric parameters of the MINC model from the specification of fracture spacing L, aperture δ, and the volume fractions f_i occupied by each interacting continuum. The volume fractions can be chosen to provide good resolution where needed, except for the constraint that the summation of fractions equals to one. Then the geometry parameters for computing the transmissibility of connection can be easily derived. Note that the fracture network permeability must be converted to an effective permeability when computing the connections between fractures or other continua. The coefficient that should be multiplied is

$$\beta = [L^2 - (L - \delta)^2]/L^2 \approx 2\delta/L \tag{1.14}$$

When the number of nested matrix cells is one, the MINC model reduces to the dual-porosity model. In this work, we apply the shape factor given by Eq. 1.6. The same shape factor is also applied for the innermost nested-cell of the MINC model. The rectangular matrix geometry chosen here is not a requirement; the model could also be extended to other matrix shapes.

It should be noted that there are other interesting alternatives to MINC such as the lumped parameter model (Zimmerman et al. 1996), or simulating diffusion in the matrix directly using appropriate analytical solutions (Geiger et al. 2013; Tecklenburg et al. 2013). We choose to apply the MINC model due to its generality. Fluid flow in unconventional reservoirs such as gas and liquid rich shale plays usually involves substantial nonlinear complexity. The flow is governed by a number of tightly coupled mechanisms including sorption, diffusion, multi-component and multi-phase flow behavior. The MINC model allows us to incorporate such physics. In addition, the MINC model is suitable for the simulation of the effects of fracturing fluid invasion, as well as the multicontinuum configuration that exists in organic-rich shale matrix. **Fig. 1.4** illustrates the coupled desorption-diffusion-advection model for an organic-inorganic-fracture configuration using MINC. This model assumes that organic matters are imbedded in an inorganic matrix.

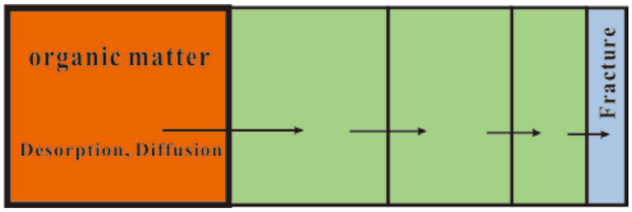

Figure 1.4: Coupled flow of MINC model with organic-inorganic-fracture configuration.

1.2 Discrete Fracture Models

1.2.1 EDFM

Lee et al. (2001), Li and Lee (2008), Hajibeygi et al. (2011) and Moinfar et al. (2012) developed and improved the embedded discrete fracture model. EDFM applies the concept of wellbore index (WI) to derive a transport index between fracture and matrix cells. Moinfar et al. (2013) show that EDFM provides adequate accuracy for multiphase compositional simulation.

Because the fractures and the matrix are modeled on different computational domains, there is no fluid communication between them in the mass balance equations. Consequently, we define non-neighboring connections (NNC) for EDFM. That is, each gridblock in the numerical model can communicate with any other gridblock through a non-neighboring connection.

The embedded fractures are discretized vertically and horizontally by the cell boundaries of gridblocks that are intersected by a fracture. Connection transmissibility is then introduced to account for the flux interaction between the fracture and the matrix. Li and Lee 2008 assume that the pressure around fracture is linearly distributed, and with this approximation the average normal distance from the fracture in the gridblock is

$$\langle d \rangle = \frac{\int \boldsymbol{n} \cdot x dS}{S} \tag{1.15}$$

where $\boldsymbol{n}$ is the unit normal vector; x is the distance from the fracture; dS and S are the areal element and area of the gridblock, respectively. Subsequently, the transmissibility is

$$T = \frac{kA}{\langle d \rangle} \tag{1.16}$$

where A is the fracture surface area in the gridblock and k is the harmonic average of the permeability of the hydraulic fracture and the matrix. For fractures that do not fully penetrate a gridblock, it is assumed that T is linearly proportional to the fracture length inside the gridblock; therefore, the transfer term between a matrix cell and a segment of a fracture embedded in that cell is

$$q_{mf} = T\left(\psi_m - \psi_f\right) \tag{1.17}$$

where q_{mf} is the volumetric rate between the matrix gridblock and the fracture segment, T is the transmissibility between them, ψ_m and ψ_f are matrix and fracture gridblock potential, respectively.

For a NNC between intersecting fracture cells, we use the same approach presented by Karimi-Fard et al. (2004), wherein the transmissibility is

$$\mathrm{T}_{ff} = \frac{T_1 T_2}{T_1 + T_2} \tag{1.18}$$

$$T_1 = \frac{k_{f1}\omega_{f1}L_{int}}{d_{f1}} \qquad T_2 = \frac{k_{f2}\omega_{f2}L_{int}}{d_{f2}} \tag{1.19}$$

where L_{int} is the length of the intersection line bounded in a gridblock, ω_f is fracture aperture and k_f is fracture permeability. Likewise, d_f is the average of normal distances from the center of the fracture subsegments (located in each side of the intersection line) to the intersection line.

Such a NNC is required for any pair of intersecting fractures. Thus, if more than two fractures intersect in a gridblock, a NNC is defined between each pair of intersecting fracture control volumes. Also, if two fractures penetrating a gridblock do not intersect with each other within the gridblock, no NNC is needed.

For a NNC between two cells of an individual fracture, k is equal to the fracture permeability and d is the distance between the centers of two fracture segments. Parameter A is the fracture aperture times the length of this intersection line.

Before fluid-flow simulation, a list of NNC pairs, the arrangement of fracture cells, the arrangement of fracture cells, the transmissibility of NNCs, and the transmissibility between fracture cells should be computed on the basis of the grid structure and fracture planes. A preprocessing code is developed to provide the required data for flow simulations.

While EDFM facilitates the modeling of irregular fracture geometry, it is not very appropriate for unconventional reservoir modeling for the reason that it assumes a linear pressure variation in the normal direction to each fracture. The extreme contrast in conductivity between fractures and the ultra-tight matrix results in steep potential gradients that are difficult to capture.

1.2.2 Unstructured DFM

Unstructured gridding provides geometric flexibility to represent irregular and non-ideal fracture geometries. In this approach, fractures are represented as lower-dimensional entities within the geometric grid, and the computational domain is expanded accordingly. Lower-dimensional DFM provides a more robust and efficient discretization compared with equal-dimensional representations that are more complexity and computationally costly due to thin cells (Karimi-Fard et al. 2004; Sandve et al. 2012).

The mesh generation method used for this study could adaptively mesh a fractured porous medium with smoothly changing meshes around fractures. The Constrained Delaunay Triangulation (CDT) is used for the whole domain, thus mesh edges are prevented from intersecting with fracture constraints. A force-equilibrium optimization algorithm is used in conjunction with CDT to provide high quality meshes around fracture tips and intersections (Holm et al. 2006). Because of the analogous force-equilibrium, mesh points will move away from each other and distributed adaptively based on the mesh size function. The force-equilibrium algorithm is based on a mechanical analogy between triangular mesh and 2-D truss structure, or an equivalent structure of springs (Persson and Strang 2004). Positions of nodes are found by solving for static force equilibrium of the truss structure. The force vector at mesh points is an array

$$\boldsymbol{F}(\boldsymbol{p}) = \left[\boldsymbol{F}_{\boldsymbol{i},\boldsymbol{x}}(\boldsymbol{p}) + \boldsymbol{F}_{\boldsymbol{e},\boldsymbol{x}}(\boldsymbol{p})\boldsymbol{F}_{\boldsymbol{i},\boldsymbol{y}}(\boldsymbol{p}) + \boldsymbol{F}_{\boldsymbol{e},\boldsymbol{y}}(\boldsymbol{p})\right] \tag{1.20}$$

where $\boldsymbol{F}_{\boldsymbol{i}}$ are the internal forces from edges, $\boldsymbol{F}_{\boldsymbol{e}}$ are the external forces from boundary reactions, $\boldsymbol{p}$ is an *N*-by-2 coordinate matrix of mesh points, and *N* is the number of mesh points.

The external forces come from reaction forces acting normal to the boundary. A linear function correspond to a linear elastic truss structure is modeled

$$f(l, l_0) = \begin{cases} k(l_0 - l), & l < l_0 \\ 0, & l \geq l_0 \end{cases} \tag{1.21}$$

where $f(l, l_0)$ is the internal force in each truss bar, l and l_0 are the actual and desired length of edge, and k is a constant unit conversion factor.

Mesh points $\boldsymbol{p}$ is then solved from the equilibrium system $\boldsymbol{F}(\boldsymbol{p}) = \boldsymbol{0}$. A pseudo time stepping method could be used

$$\frac{d\boldsymbol{p}}{dt} = \boldsymbol{F}(\boldsymbol{p}), \quad t \geq 0 \tag{1.22}$$

Eq. 1.22 is then discretized explicitly using the forward Euler method

$$\boldsymbol{p}(t_{n+1}) = \boldsymbol{p}(t_n) + \Delta t \cdot \boldsymbol{F}\big(\boldsymbol{p}(t_n)\big) \tag{1.23}$$

after each time step, new mesh points $\boldsymbol{p}(t_{n+1})$ are updated from the pre-step positions $\boldsymbol{p}(t_n)$, and new triangulation is generated by the CDT algorithm using $\boldsymbol{p}(t_{n+1})$**.** Finally, the iteration terminates if norm of $\boldsymbol{F}\big(\boldsymbol{p}(t_{n+i})\big)$ comes close to zero.

We need to calculate the transmissibilities for the matrix-matrix, matrix-fracture, and fracture-fracture block pairs. We follow the method developed by Karimi-Fard et al. (2004), which we now describe.

For matrix-matrix transmissibility, suppose that blocks 1 and 2 are part of the matrix, with the average pressures in them being P_1 and P_2. According to Darcy's law, the volume flow rate q_{12} between the two blocks is given by $q_{12} = T_{12}(P_2 - P_1)$. The transmissibility

$$T_{12} = \frac{\alpha_1 \alpha_2}{\alpha_1 + \alpha_2} \tag{1.24}$$

and the flow conductance

$$\alpha_i = \frac{A_i K_i}{D_i} \boldsymbol{n_i} \cdot \boldsymbol{f_i} \tag{1.25}$$

being a flow conductance. A_i is the common face between the two triangles, K_i the absolute permeability of triangle i, D_i the cell-to-face distance of block i, $\boldsymbol{n_i}$ the vector normal to the face pointing toward block i, and $\boldsymbol{f_i}$ the unit vector parallel to the cell-to-face connecting the line pointing toward block i. In effect, the two conductances α_1 and α_2 are in series, and T_{12} is simply the equivalent flow conductance.

Fracture-fracture transmissibility could be calculated as in Eq. 1.18. We apply the *star-delta transformation* (Karimi-Fard et al. 2004) for fracture intersections. This formulation allows for different face areas and face normal vectors on either side of the connection, in addition to handling intersecting fractures without introducing intermediate cells. The transmissibility of each connection at the fracture intersection is

$$T_{12} = \frac{T_1 T_2}{\sum_{i=1}^{\eta} T_i} \tag{1.26}$$

where η is the number of intersecting fracture segments.

The procedure for computing the transmissibility between a matrix block and a fracture is the same as that for the matrix-matrix blocks and, therefore, need not be repeated. In order to simplify the grid generation algorithm, no volume is assigned to the fractures. During the fluid flow simulations, however, each fracture has its own volume (thickness and length), i.e., taken into account in the mass balance calculations. Doing otherwise will generate errors in the volume calculations, which can be considerable if there are many fractures in the computational grid. To avoid the error, the volume of each fracture is subtracted from that of its adjacent matrix.

CHAPTER 2

HYBRID COUPLED DISCRETE FRACTURE-MATRIX AND MULTICONTINUUM MODELS

Hybrid models that can effectively integrate DFM with continuum-type approaches are a promising direction towards the accurate and efficient modeling of multi-scaled stimulated unconventional formations. In this work, we develop two types of hybrid technique that could be utilized for different applications depending on the available characterization data and the different requirements for efficiency and accuracy considerations.

The first hybrid model that we propose couples EDFM with MINC (EDFM-MINC) in order to simulate the stimulated reservoir volume (SRV) for hydraulically fractured tight- and shale plays when detailed fracture characterization data for the small scale fractures is not available. This optimized model could reduce the computational cost that is associated with the widely applied logarithmically spaced, locally refined gridding strategy (Cipolla et al. 2009; Rubin 2010; Hinkley et al. 2013; Wilson and Durlofsky 2013), while improving the flexibility to model complex hydraulic fracture geometry. The hybrid model could be used for long-term well performance evaluation in order to obtain a balance between accuracy and computational efficiency. It is also suitable for well interaction analysis and well placement studies that involve numerous wells and dozens of hydraulic fracture clusters with complex configurations. In this work, the EDFM-MINC approach is validated by comparison to solutions from the refined single-porosity reference model.

In the second class of hybrid model (UDFM-MINC), the primary fractures are described using DFM with unstructured triangular grids, and the small-scale fractures are simulated by continuum-type approaches in a fully coupled manner. Optimized local grid refinement (LGR) is employed to accurately handle the transient flow regime around primary fractures. Moreover, an upscaling technique is developed in order to capture the complex natural fracture geometry using a dual-permeability (DK) model. The upscaling technique employs EDFM on the detailed realization of the DFN using the target unstructured grid in order to generate an appropriate DK model. This hybrid approach does not rely on the assumption of an idealized geometry of the fracture network that is typically made by traditional dual-continuum approaches; thus it is applicable to cases where a detailed prior model for the complete fracture network is available. The potential gradient associated with the fracture and matrix continua could also be resolved using the refined gridding around primary fractures.

We first summarize the physical model, governing equations, and base finite-volume discretization that are used throughout this paper. This chapter is organized as follows: first, we review the basic building blocks of the proposed hybrid methods and we present the rationale for these choices. Next, we develop the two proposed hybrid methods and the associated upscaling procedure. This is followed by the validation studies that are aimed at illustrating the strengths and weaknesses of the two hybrid models. Finally, we present further simulation examples and sensitivity studies.

2.1 Physical Model

We develop a two-phase (gas, water) simulator which incorporates storage and transport mechanisms to modeling unconventional gas reservoirs. All the simulation studies for demonstrating the applications of our hybrid fracture models are performed using this simulator. We describe gas properties with real-gas option (density and viscosity), and apply two sets of relative permeability and capillary pressure curves to matrix and fracture. The developed hybrid fracture models could also be used for simulating other unconventional resources such as coal-bed methane, tight/shale oil reservoir, etc.

The finite-volume formulation which is very flexible for handling interactions between various kinds of continua is applied for discretizing the governing equations. Time discretization is carried out using a backward, first-order, fully implicit FD scheme. The corresponding Jacobian matrix is evaluated by Automatic Differentiation with Expression Templates Library (ADETL), which provides a numerical framework allowing wide flexibility in the choice of variable sets and generic representations of discretized expressions for gridblocks.

2.1.1 Apparent Permeability

Unconventional gas formations are believed to be comprised of pores that are at the nanoscale, ranging in size from one to hundreds of nanometers. Conventional Darcy’s law does not adequately describe the various non-viscous gas flow regimes that may be present. Darcy's law is valid under the assumption of continuum flow, and as the length-scale of the pore throat diameters approaches the mean-free-path of the gas molecules, the continuum assumption does not apply (Javadpour et al. 2007). In this paper, we implemented the transport model proposed by Florence et al. (2007) in our numerical simulator. The general form of the model includes an apparent permeability correction for gas transport in nano-scale porous media

$$F_{app} = \frac{k_{app}}{k_D} \tag{2.1}$$

where F_{app} is the correction factor for apparent permeability.

Florence et al. (2007) extended the derivation of Karniadakis et al. (2001) to the following form that relies only on the Knudsen number K_n, and the Darcy permeability

$$F_{app} = (1 + \alpha_K K_n)\left(1 + \frac{4K_n}{1 + K_n}\right) \tag{2.2}$$

the Knudsen number is

$$K_n = \frac{\bar{\lambda}}{r} = \frac{\mu_g}{2.81708 p_g}\sqrt{\frac{\pi RT}{2M}\frac{\phi}{k_D}} \tag{2.3}$$

the term α_K in Eq. 2.2 is the rarefaction parameter

$$\alpha_K = \frac{128}{15\pi^2} tan^{-1}(4K_n^{0.4}) \tag{2.4}$$

where $\bar{\lambda}$ is the mean free path of gas molecules; μ_g is the gas viscosity; p_g is the gas phase pressure; R is the gas constant; T is the temperature; M is the molecular weight.

2.1.2 Governing Equations

Although what we are most concerned with in unconventional gas reservoir simulations is to model gas flow from reservoir to well, water phase flow is often occurring simultaneously with gas flow because of the existence of hydraulic fracturing fluids or the mobile in-situ connate water (Wu et al. 2013). The dynamics of the water phase also need to be accurately simulated for water invasion and water blocking effect. We consider two-phase system in a porous media which fills the domain $\Omega \subset \mathbb{R}^n, n = 2, 3$. The model assumes gas is stored in natural and primary fractures as free phase, while in matrix as both free and adsorbed phase. The governing equations are the conservation of molar mass for each phase $\alpha = g, w$

$$\frac{\partial}{\partial t}\left[\phi \rho_g S_g + (1-\phi) m_g\right] + \nabla \cdot \left(F_{app} \rho_g \boldsymbol{u}_g\right) = \Psi_g^{conn} + q_g^W \tag{2.5}$$

$$\frac{\partial}{\partial t}(\phi \rho_w S_w) + \nabla \cdot (\rho_w \boldsymbol{u}_w) = \Psi_w^{conn} + q_w^W \tag{2.6}$$

We consider the gas adsorption m_g described by Langmuir isotherm in the accumulation term, and multiply apparent permeability correction F_{app} with the flux term to consider gas diffusion and slippage. Ψ_α^{conn} denotes the mass communication between different domains (matrix, natural-/micro-fracture, primary fracture), and it has the similar expression as flux term. Eqs. 2.5/2.6 are applicable for different domains, with slight difference that we neglect adsorption and apparent permeability for fracture medium. Eqs. 2.5/2.6 need to be completed with constitutive relations, and initial conditions as well as boundary conditions of Neumann or Dirichlet type. Darcy's law is used for the phase velocity

$$\boldsymbol{u}_\alpha = -\frac{k k_{r\alpha}}{\mu_\alpha}(\nabla p_\alpha - \gamma_\alpha g \nabla D) \tag{2.7}$$

the source/sink term for phase α is

$$q_\alpha^W = \frac{k_{r\alpha}}{\mu_\alpha} \rho_\alpha (p_\alpha - p^W) \tag{2.8}$$

the saturation and capillary pressure constraints are

$$S_g + S_w = 1 \tag{2.9}$$

$$p_c(S_w) = p_g - p_w \tag{2.10}$$

where $\alpha = \text{water}, \text{gas}$; S_α is the saturation; $k_{r\alpha}$ is the phase relative permeability; γ_α is the phase mass density; p^W is the well bottom-hole pressure; ρ_α is the phase molar density; μ_α is the phase viscosity; m_g is the molar mass of gas adsorbed in unit formation volume; $\boldsymbol{u}_\alpha$ is the phase velocity; Q_α^W is the source/sink term of phase α; Ψ_α^{conn} is the flux term of phase α between domains; p_c is the capillary pressure between water and gas phase.

The gas density is computed as a function of pressure at isothermal conditions using the Peng-Robinson Equation Of State (PR-EOS). The model derived by Lee et al. (1966) is used for calculating gas viscosity in this work. The expressions of relative permeability and capillary pressure are from Ho and Webb (2006).

2.1.3 Finite-Volume Discretization

The finite-volume approach provides a general spatial discretization scheme that can represent a three-dimensional domain using a set of discrete meshes. The transport and storage properties in each mesh are represented by proper averaging over certain control volume, while fluxes of mass across surface segments are evaluated through finite difference approximations (Pruess et al. 1985). A two-point flux approximation (TFPA) is used to compute the flux at an interface shared between two control volumes. It is assumed that pressure varies linearly within each of the two control volumes. The total face transmissibility that combines two half-transmissibilities in a harmonic average for the flux term is

$$T_j = \frac{T_i T_k}{T_i + T_k} \tag{2.11}$$

the two-point half-transmissibility for a general unstructured mesh is obtained by imposing flux and potential continuity at the center of the interface (Moog 2013)

$$T_i = \frac{\boldsymbol{d}_i \cdot (\mathbf{K}_i \cdot \boldsymbol{n}) A_j}{|\boldsymbol{d}_i|^2} \tag{2.12}$$

where $\boldsymbol{n}$ is the unit normal to the face; A_j is the interface area; $\mathbf{K}_i$ is the permeability tensor for the i^{th} control volume (we assume isotropic permeability in this work); $\boldsymbol{d}_i$ is the vector from the centroid of cell $\boldsymbol{i}$ to the centroid of the face. The schematic for computing T_i is shown in **Fig. 2.1**.

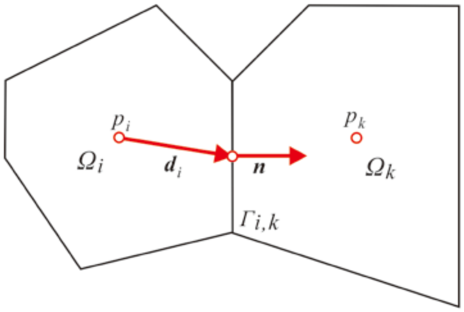

Figure 2.1: Schematic for computing the two-point transmissibility.

It should be noted that some accuracy issue inherent in two-point type discretization may arise due to the grid non- orthogonality (Aavatsmark 2002; Lie et al. 2012). The details for the discretized equations obtained by finite-volume scheme won't be shown in this paper. Here we only provide the expression for the well term of multi-fractured horizontal well. We assume that the reservoir fluid only flow from hydraulic fractures into the wellbore, and there's no pressure drop along the horizontal wellbore.

$$Q_\alpha^W = WI_F \frac{k_{r\alpha}}{\mu_\alpha} \rho_\alpha (p_\alpha - p^W) \tag{2.13}$$

For a transverse fracture that intersects with horizontal wellbore in a gridblock, we could adapt the Peaceman's well model to compute the well index WI_F which relates the wellbore pressure to the pressure of the corresponding fracture control volume, as (Moinfar et al. 2012)

$$WI_F = \frac{2\pi \omega_F k_F}{ln(r_o/r_w)} \tag{2.14}$$

$$r_o = 0.14\sqrt{L_F^2 + h_F^2} \tag{2.15}$$

where ω_F is the fracture aperture (equal to the length of the well intercepted by a transverse fracture); L_F is the fracture length bounded in the gridblock, and h_F is the fracture height in the same block; k_F is the fracture permeability; r_w is the wellbore radius.

2.2 Proposed Hybrid Models and An Associated Upscaling Process

We develop two alternate hybrid models that are aimed at combining the advantages of multicontinuum and DFM representations. The objectives are to:

1. Represent realistic complex fracture geometry;
2. Adequately capture sharp local potential gradients due to severe permeability contrasts;
3. Allow for the incorporation of apparent permeability and other transport mechanisms, and;
4. Reduce the computational cost of representing naturally fractured systems.

2.2.1 Hybrid Model I: EDFM-MINC

The first hybrid model combines MINC with EDFM. The MINC concept serves two purposes. Firstly, it is used to represent a dense and well-connected small-scale/natural fracture network that is activated by stimulation job. Secondly, it allows the method to handle the extreme contrast in conductivity between small-scale/natural fractures and ultra-tight matrix that results in steep potential gradients. EDFM is used to represent sparse irregular primary fractures. Note that large potential gradient will not exist in the fracture network because the conductivity contrast between primary fracture and small-scale/nature fracture is not so distinct. Subsequently, satisfactory results could be obtained under the assumption of uniform pressure over the fracture network faces in the hybrid model.

The proposed hybrid model provides flexibility in the communication between primary fractures and the small-scale/nature fracture network according to the multicontinuum concept (Jiang et al. 2014). We assume that the primary fracture first interacts with the fracture medium of the MINC model. Direct mass transfer to the primary fracture from the matrix medium is neglected. **Fig. 2.2** illustrates a connection list dependency of continua in a computational domain for a simple scenario that has a single matrix nested cell. The key aspect of the hybrid model is the calculation of the connection transmissibility for flux interaction between different domains. The mass transfer of phase α between the fracture network in the MINC model and primary fracture is expressed as (f: fracture network; F: primary fracture)

$$Q_{\alpha}^{fF} = T_{fF} \beta \frac{k_{r\alpha}}{\mu_{\alpha}} \rho_{\alpha} \left(p_{f\alpha} - p_{F\alpha} \right) \tag{2.16}$$

Eq. 1.16 is used for computing the transmissibility T_{fF}, and is modified so that k is the harmonic average for the permeability of f and F. The conversion coefficient β in Eq. 1.14 should also be multiplied for the fracture network.

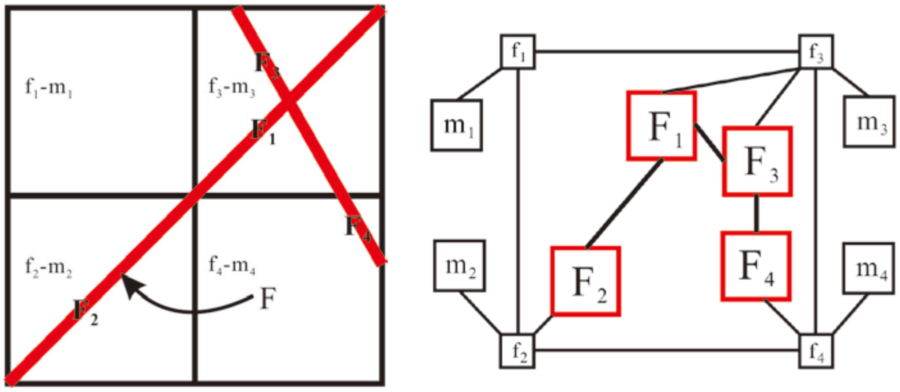

Figure 2.2: Example of the connection list for EDFM coupled with MINC.

2.2.2 Hybrid Model II: UDFM-MINC

Current hybrid models appearing in the literature are not applicable to unconventional scenarios. The hybrid model developed by Wu et al. (2013) lacks the flexibility to handle complex fracture geometries due to the use of structured gridding. Another hybrid model (Moinfar et al. 2013) applies EDFM to describe primary fractures but cannot capture the extreme potential gradient in the ultra-tight matrix around primary fractures because suitable LGR technique is not available.

A coupled method is developed to integrate unstructured DFM with continuum-type models (dual-porosity, dual-permeability, as well as MINC). Predefined distance functions are employed for optimal LGR feature around the primary fractures. This hybrid model could provide high-resolution solutions for transient behavior characterization. The schematic of the grid (lower-dimensional) and the computational domain for such a hybrid model is shown in **Fig. 2.3**.

The effective flow properties for the matrix and fracture network continuum in the hybrid model could be obtained by the same procedure for computing the parameters of continuum-type models (assume regular fracture network as shown in **Fig. 1.2**). They could also be generated by the unstructured upscaling method which will be introduced in the following discussion.

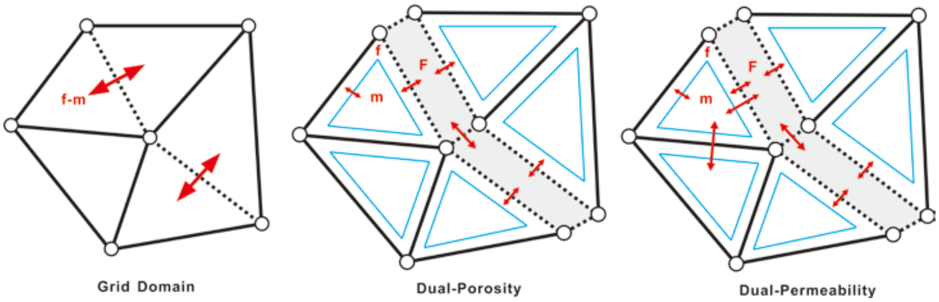

Figure 2.3: Grid domain and computational domain for the hybrid model.

2.2.3 Unstructured Dual-Permeability (DK) Upscaling Method

Recent advances in micro-seismic mapping technology and hydraulic fracturing modeling of fracture propagation provide insights that indicate a surprising level of complexity in hydraulically-created fracture networks in unconventional formations. These complexities arise from the heterogeneity of mechanical rock properties and the interaction of hydraulic fractures with pre-existing natural fractures. Fracture characterization data (outcrop, core, image log analysis, and seismic, etc.) could be assimilated to stochastically generate multiple realizations of discrete fracture network (DFN). Assumption of a well-connected, orthogonal fracture network with idealized distribution is often not applicable. A direct fine-scale model where fractures at all length scales are resolved is impractical from a computational perspective. Upscaling procedures are necessary in order to construct a corresponding multicontinuum model from a particular discrete fracture characterization.

In this work, the upscaling method proposed by Moinfar et al. (2013) is extended and implemented within the hybrid fracture model based on unstructured grid without invoking traditional DP simplifications. Optimized LGR is employed near primary fractures that are described by an unstructured DFM. Although the upscaling procedure could only construct the corresponding DK model, the potential gradient in the fracture- and matrix-continuum could be resolved to some extent by the detailed gridding around primary fractures.

Compared with flow-based upscaling methods, our method has the advantages of reduced computational cost, and of entirely bypassing the challenges in gridding the fine scale model. However, the multiple sub-region (MSR) method (Karimi-Fard et al. 2006; Gong et al. 2008) is a promising alternative to the upscaling procedure for our hybrid fracture model. MSR entails the construction of flow-based MINC model for each coarse block from the detailed DFM, providing higher efficacy to capture the matrix dynamics.

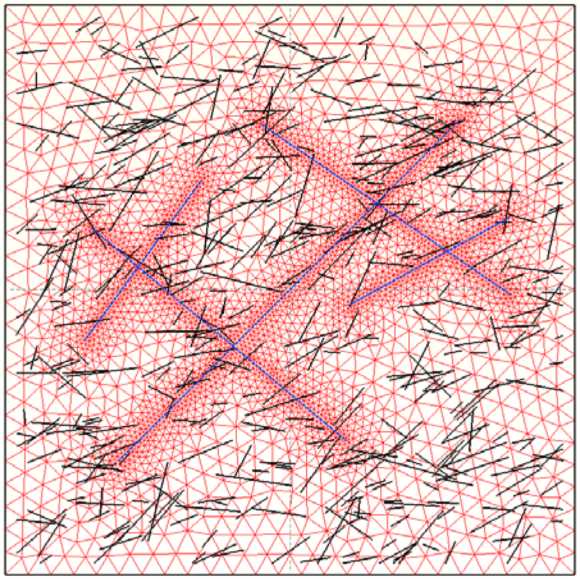

Figure 2.4: Schematic of unstructured gridding and embedded fracture network in the hybrid model.

We aim to maintain the advantages of the continuum-type models without losing the dominant role of primary fractures as fluid conduit connecting reservoir with wellbore. One critical step for fulfilling hybrid fracture modeling is to set the scale criterion for different levels of fractures. The criterion for classification should be able to identify the primary fractures that will exhibit significant potential gradient and have a large impact on the transient flow regime during production process. Criterions such as the connectivity with hydraulic fractures, length and conductivity could be considered. Different levels of fractures will be simulated by models with different levels of details (discrete or continuum). The fracture network pattern with a multi-scaled nature could be established from fracture characterization data and hydraulic fracturing models for unconventional stimulated well (Cipolla et al. 2011). **Fig. 2.4** shows an example for the schematic of unstructured gridding and embedded fracture network (primary fracture: blue line; natural fracture: black line) in our hybrid model.

A preprocessing routine is developed to compute the connection lists and transmissibilities between different types of fracture and matrix domain. The subscripts m, f, and F in the following discussion refer to the cells in the matrix, continuum-fracture and discrete-fracture domains, respectively. In order to calculate the transport parameters of the continuum-fracture domain in our hybrid model, upscaling procedure should be introduced. The transmissibility between a matrix cell and the corresponding continuum-fracture cell is a weighted sum of transmissibility of each embedded fractures with the matrix (Moinfar et al. 2013)

$$T_{m-f} = \sum_{i=1}^{N_f} w_i \, T_{m-f,i} \tag{2.17}$$

where N_f is the number of embedded natural fractures in the gridblock, w_i is the volume of the i-th fracture bounded in that gridblock divided by the total volume of fractures in that cell, and $T_{m-f,i}$ is the transmissibility of the i-th fracture with the matrix gridblock. The schematic for the $f-f$, $F-f$ connections are shown in **Fig. 2.5**, and the transmissibilities could be calculated in a similar weighted sum.

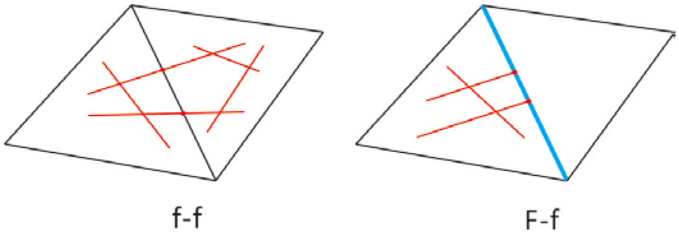

Figure 2.5: Schematic for the f-f, F-f connections.

The transmissibility $T_{m-f,i}$ between embedded natural fracture and matrix is calculated by Eq. 1.16. We assume that matrix pressure varies linearly from the fracture to the block boundaries. Following this assumption, the average pressure in a matrix block is related to the average normal distance from the fracture. The average normal distance $\langle d \rangle$ is normally calculated by numerical method. However, for most cases, analytical solutions could be obtained for reducing the computational cost. For instance, $\langle d \rangle$ of an embedded fracture intersecting with a triangular matrix could be computed as an integral form

$$\langle d \rangle = \frac{\int \boldsymbol{n} \cdot x dS}{S} = \frac{\int_{X_{L1}}^{X_{U1}} \int_{Y_{L1}}^{Y_{U1}} d\, dydx + \int_{X_{L2}}^{X_{U2}} \int_{Y_{L2}}^{Y_{U2}} d\, dydx}{S} \tag{2.18}$$

$$X_{U1} = x_3\,,\ \ X_{L1} = x_1\,,\ \ X_{U2} = x_2\,,\ \ X_{L2} = x_3 \tag{2.19}$$

$$\begin{aligned} Y_{U1} &= y_1 + \frac{y_1 - y_2}{x_1 - x_2}(x - x_1),\ Y_{L1} = y_1 + \frac{y_1 - y_3}{x_1 - x_3}(x - x_1), \\ Y_{U2} &= y_1 + \frac{y_1 - y_2}{x_1 - x_2}(x - x_1),\ Y_{L2} = y_3 + \frac{y_2 - y_3}{x_2 - x_3}(x - x_3) \end{aligned} \tag{2.20}$$

$$d = \frac{|(y_b - y_a)x - (x_b - x_a)y + x_b y_a - y_b x_a|}{\sqrt{(y_b - y_a)^2 + (x_b - x_a)^2}} \tag{2.21}$$

where S is the triangle area; d is the distance of a point from the fracture line. The triangle vertices and the intersecting points are shown in **Fig. 2.6**. For the matrix gridblock with rectangular shape, the expression for calculating $\langle d \rangle$ becomes simpler.

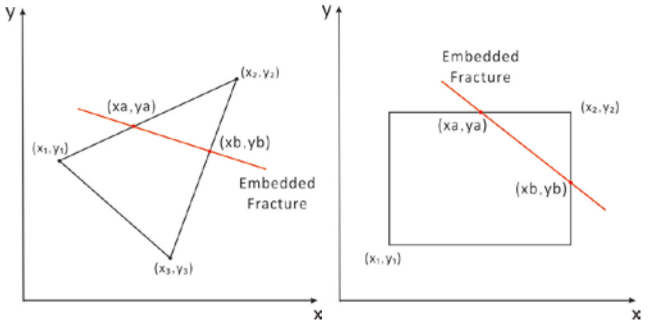

Figure 2.6: Schematic for an embedded fracture intersecting with matrix gridblock.

Currently, the first hybrid model (EDFM+MINC) we developed could simulate 3D scenario, but the primary fracture described by EDFM are limited to vertical direction (no inclination). For the second hybrid model, all the implementations are 2D, and could be extended to 2.5D model which contains multiple layers in z-direction with trivial effort. The challenges associated with the extension to 3D would mostly lie on the identification of object intersection and the creation of connection-list from computational geometry aspect. The average normal distance for 3D geometry could be calculated analytically in a similar manner with 2D without difficulty.

2.3 Model Validation

2.3.1 Problem 1: Linear Gas Flow of Fractured Well at Constant BHP

Chen and Raghavan (2013) derived a semi-analytical solution for the gas transient flow in a one-dimensional reservoir with a fractured well produced at constant pressure using the concept of pseudo-pressures. Due to the steepness of pressure drops from the ultra-low permeability matrix to the high-conductivity hydraulic fractures, strong nonlinearities associated with the gas properties would exist. To verify the numerical solutions presented in this paper, we compared our simulator with the semi-analytical solution in the presence of large permeability contrast between matrix and fracture.

The fracture is simulated by the EDFM based on structured grid. The data used in the simulation of this validation problem appear in Table 2.1. We implement the correlations from Azizi et al. (2010) for the gas compressibility factor, and Lee et al. (1966) for gas viscosity.

Simulations are performed with a different number of gridblocks (161, 401, 1001, 2001, and 4001). The log-log plot for the gas rate over time of the analytical and numerical solution is shown in **Fig. 2.7**. Only slight differences are observed at the early period using the coarsest simulation model. Note that the semi-analytical solution is valid for infinite-acting flow, which results in the decrease of numerical result at the late boundary flow. We also compare the relative error between the analytical and numerical solutions for different cases to examine the grid sensitivity. The relative error

$$\varepsilon_N = \frac{max(|q_a(t) - q_N(t)|)}{max[|q_a(t)|, 1]} \tag{2.22}$$

The results appear in **Fig. 2.8**. A quadratic relationship between the number of gridblocks and the relative error is observed.

Table 2.1: Parameters for Problem 1.

x_f (m)	h (m)	k_m (m^2)	ϕ_m	L (m)	p_i (MPa)	p_{wf} (MPa)	SG	T (K)
30.48	30.48	1.0e-	0.06	80	48.26	3.45	0.65	366.48

where x_f is the fracture length; h is the fracture height; k_m is the matrix permeability; ϕ_m is the matrix porosity; L is the model length; p_i is the initial pressure; p_{wf} is the fracture pressure; SG is the gas gravity; T is the temperature.

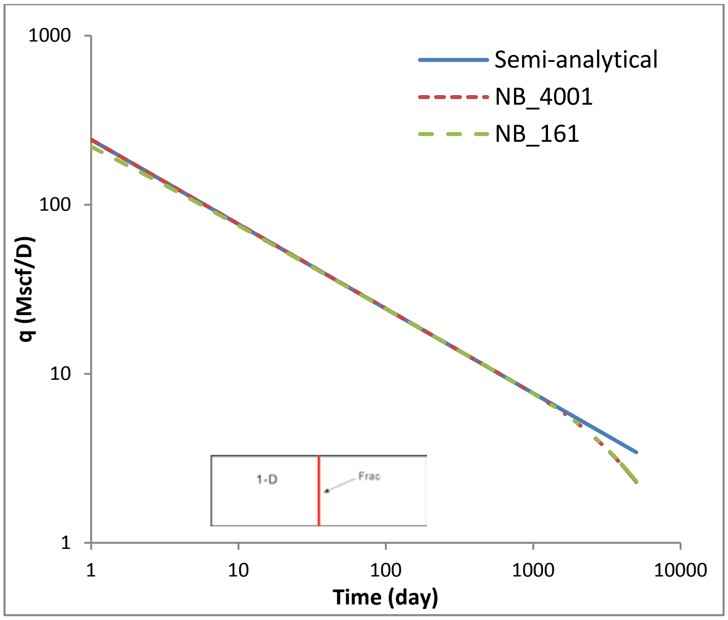

Figure 2.7: Gas rate of the semi-analytical and numerical solution (with 161, 4001 number of gridblocks).

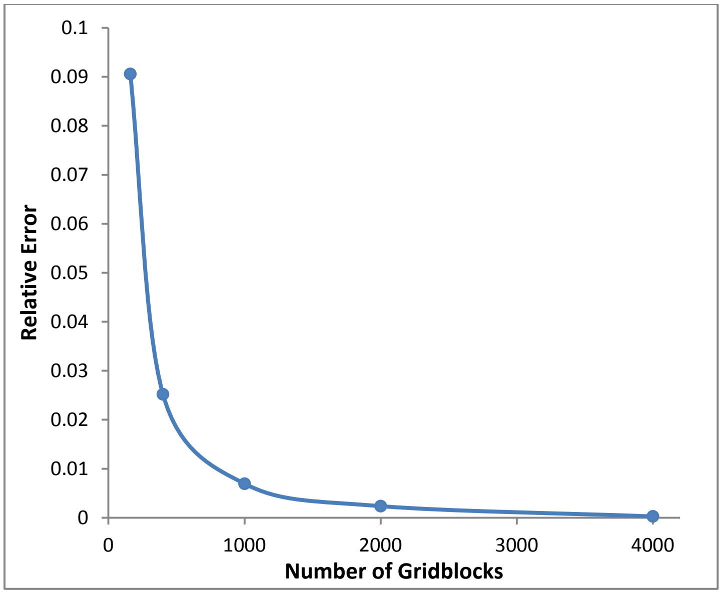

Figure 2.8: Relative error versus number of gridblocks.

2.3.2 Problem 2: Two-Dimensional Transient Flow with Multiple Hydraulic Fractures

We apply the solution of Ozkan and Raghavan (1991) to describe liquid flow from a rectangular reservoir into infinite-conductivity vertical fractures. Uniform flux is assumed at the fracture surface. The EDFM based on unstructured triangular grid is used to simulate the fractures, and we compare the case with three fractures at the reservoir center. The reservoir is discretized into 10351 triangular gridblocks. The parameters used in the validation problem are summarized in Table 2.2. Due to the coarse grid we employ around fractures, the matrix permeability of the model is set to be high. For the cases with ultra-low matrix permeability, LGR is still needed to capture the large potential gradient. **Fig. 2.9** shows the log-log plot of dimensionless pressure and pressure derivatives versus dimensionless time of the semi-analytical and numerical solutions. As can be seen, the fracture model based on unstructured EDFM could capture various flow regimes (linear, pseudo-radial, and boundary-dominant flow), and transient pressure behavior with acceptable accuracy.

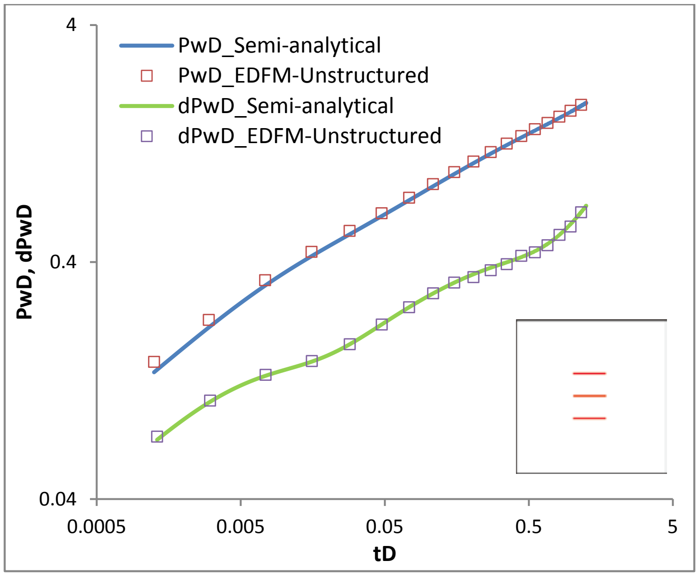

Figure 2.9: Comparison result for pressure and pressure derivative between semi-analytical and numerical solution.

Table 2.2: Parameters for Problem 2.

k (m^2)	ϕ	μ $(Pa.s)$	C_t (Pa^{-1})	Q (m^3/s)	h (m)	x_e (m)	y_e (m)	x_f (m)	L_f (m)
1.0e-14	0.4	1.0e-3	1.0e-9	1.0e-4	20	600	800	30	100

where x_e, y_e is the reservoir length and width; x_f is the fracture half-length; L_f is the fracture spacing.

2.3.3 Problem 3: Hybrid Fracture Model I (EDFM-MINC)

In order to validate the first proposed hybrid model, we compare simulation results with those obtained using a LS-LR model. The model parameters are summarized in Table 2.3. One primary fracture described by EDFM is in the middle of the reservoir and its length is the same with the reservoir length in y direction. The model is 2-dimensional and the formation is fully penetrated by the vertical fractures. The flow model is single-phase (gas) without any special mechanisms such as desorption or diffusion. The stimulated area contains 10×5 number of fracture network blocks. We use the same logarithmic-scale for both gridding in the hybrid and reference model.

Table 2.3: Parameters for Problem 3.

Parameter	Value	Unit
Fracture network blocks	10×5	
Formation thickness	20	m
Initial reservoir pressure	16	MPa
Temperature	343.15	K
Matrix porosity	0.1	
Number of matrix nested-cells	7	
Primary fracture permeability	5.0e-12	m^2
Fracture porosity	1.0	
Fracture width	4.0e-3	m
Fracture network spacing	10 /30 /60	m
Well radius	0.1	m
Producer BHP	4	MPa

Table 2.4: Permeability of matrix and fracture network for the three cases.

Case	Matrix	Fracture network
1	1.0e-20	5.0e-14
2	1.0e-19	5.0e-14
3	1.0e-19	5.0e-13

Table 2.5: Number of gridblocks for the hybrid and reference models and CPU time ratio.

	MINC blocks	Number of gridblocks	CPU time ratio
Hybrid	10 × 5	400	1:33
	20 × 10	1600	1:9
	30 × 15	3600	1:4
Reference		11476	1:1

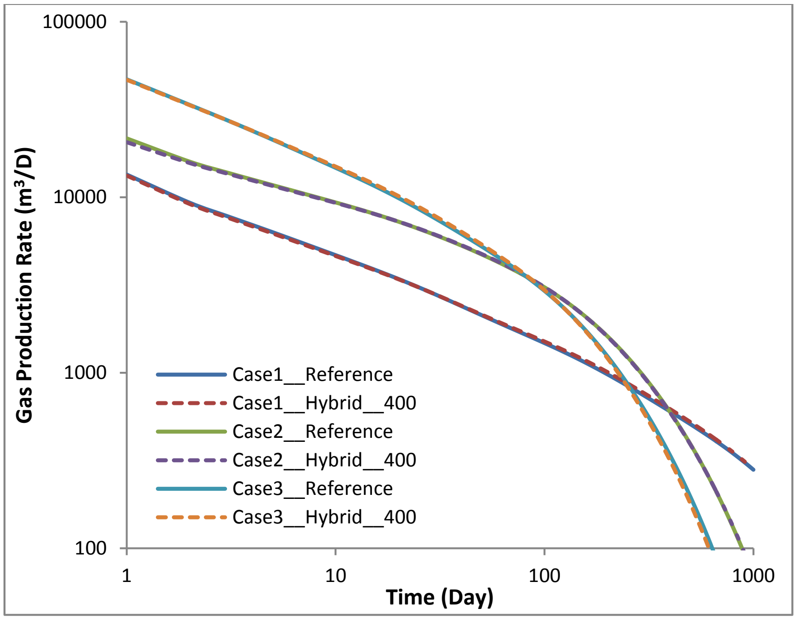

Figure 2.10: Comparison result for the gas rates of 10m fracture spacing.

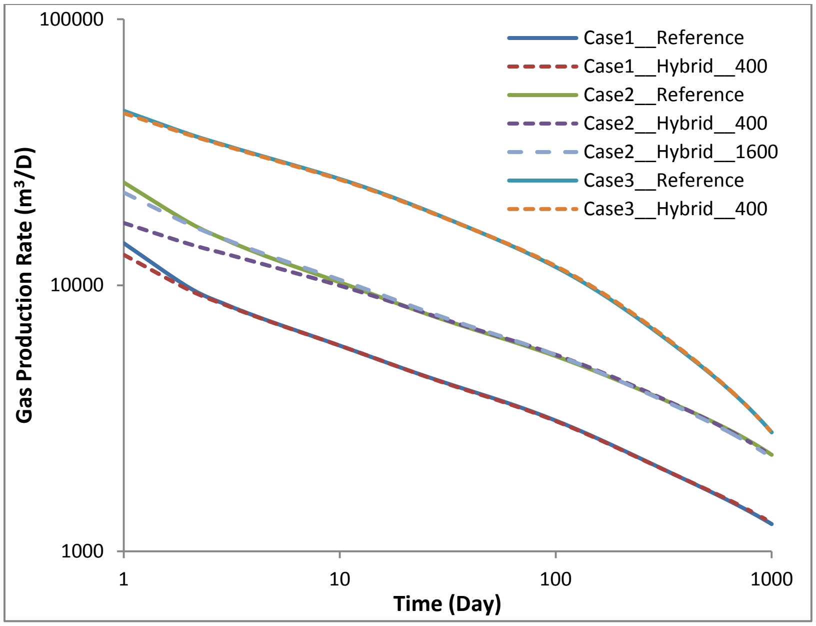

Figure 2.11: Comparison result for the gas rates of 30m fracture spacing.

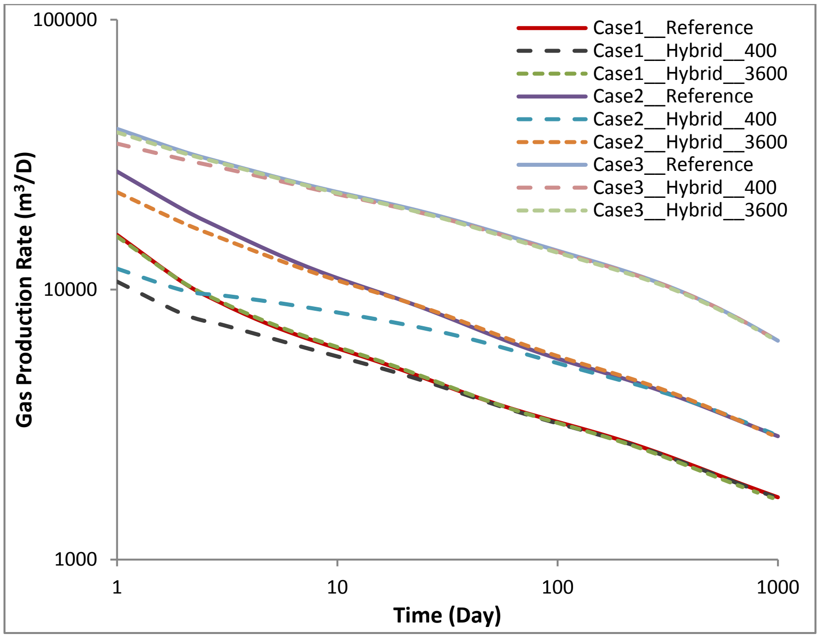

Figure. 2.12: Comparison result for the gas rates of 60m fracture spacing.

We run three cases with different fracture network spacing (10/30/60m). For each case, we compare the results for different matrix and fracture network permeability to represent the typical value range for a fractured shale-gas reservoir (shown in Table 2.4). The log-log plots for the gas rates obtained from the hybrid and reference models are shown in **Figs. 2.10/2.11/2.12**. The results show that the hybrid model with the coarse grid (400 gridblocks) could match the reference model accurately for most cases.

However, for the cases with large spacing and small permeability of the fracture network, large discrepancies in gas rates are observed at the early production period. This indicates that in such scenarios, having one fracture cell per fracture network block for the hybrid model is not adequate to properly resolve the pressure variation in the fracture. Therefore we simply refine the MINC gridblocks for higher resolution within the fracture network, and then the results with acceptable accuracy are obtained. Moderate level of local grid refinement (LGR) could also be employed around the primary fracture to optimize the total number of simulation gridblocks (MINC gridblocks).

The total simulation time is 1000 days with a constant 1 day time step size. The number of gridblocks for the hybrid and reference models, and the ratios of the elapsed CPU time for the hybrid model to the reference model are summarized in Table 2.5. In general, the hybrid model could substantially reduce gridblock quantity compared with the reference model, and thus greatly improve the computational efficiency.

2.3.4 Problem 4: Hybrid Fracture Model II (Unstructured DFM)

A synthetic model is generated to contain a single-stage hydraulically-fractured horizontal well in the center of a reservoir with a complex primary fracture network. The model also incorporates a natural fracture DFN that is stochastically generated using a Monte-Carlo simulation technique. Log-normal prior models are applied for the parameters of the natural fracture system; length, orientation, density, and location. The specifications of the model appear in Table 2.6, and unlisted parameters remain the same as in Table 2.3. We consider two-phase (gas and water) flow with no storage or non-standard transport mechanisms. The parameters for relative permeability and capillary pressure are summarized in Tables 2.7 and 2.8.

Table 2.6: Parameters for Problem 4.

Parameter	Value	Unit
Reservoir dimensions (x,y,z)	100, 100, 10	m
Initial reservoir pressure	14	MPa
Initial water saturation	0.4	
Fracture porosity	0.8	
Matrix permeability	5.0e-19	m^2
Water viscosity	5.0e-4	$Pa.s$
Water compressibility	4.3946e-10	$1/Pa$
Matrix compressibility	1.0e-9	$1/Pa$
Fracture compressibility	1.0e-8	$1/Pa$
Natural fracture width	3.0e-4	m
Hydraulic fracture width	3.0e-3	m
Natural fracture permeability	5.0e-14	m^2
Hydraulic fracture permeability	5.0e-12	m^2

Table 2.7: Parameters for relative permeability.

Irreducible water saturation S_{lr}	0.15
Exponent λ	0.45
Irreducible gas saturation S_{gr}	0.05

Table 2.8: Parameters for capillary pressure.

	Shale matrix	Fractures
Irreducible water	0.05	0.05
Exponent λ	0.45	0.55
P_0 (Pa)	1.0×10^5	5.0×10^4

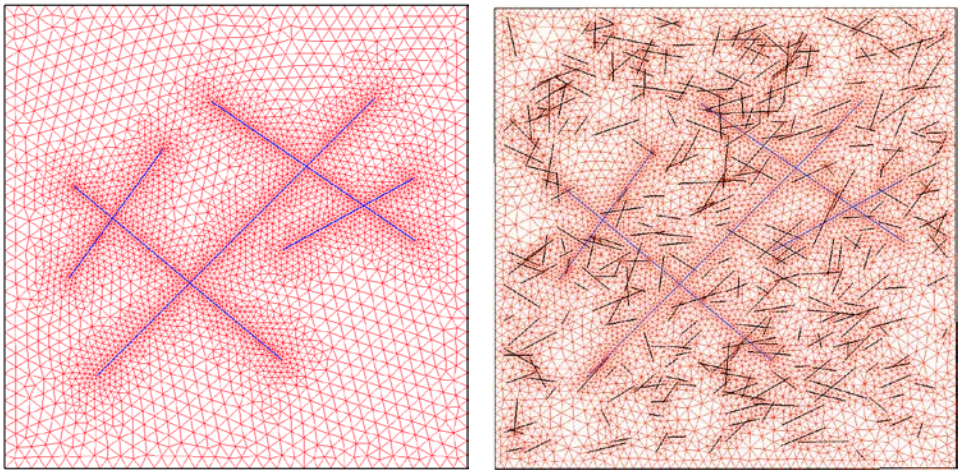

Figure 2.13: Schematics for the hybrid (9916) and reference (fine-scale) model.

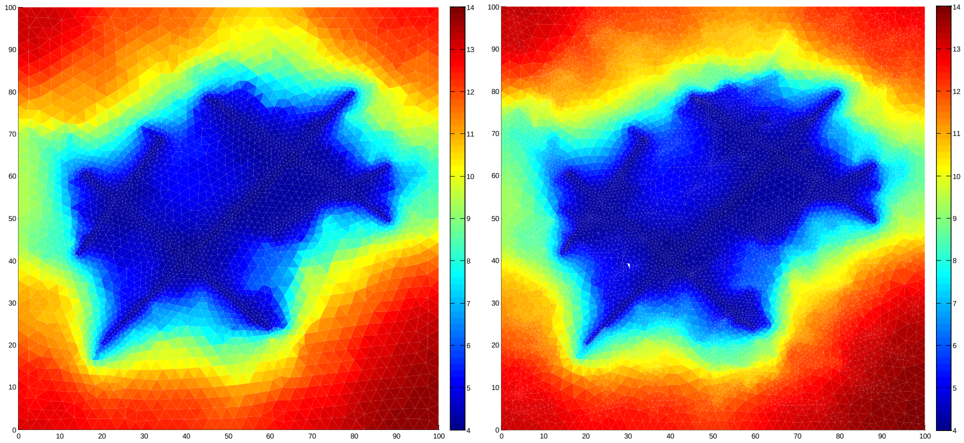

Figure 2.14: Pressure profile of the matrix at 600day for the hybrid (9916) and reference model.

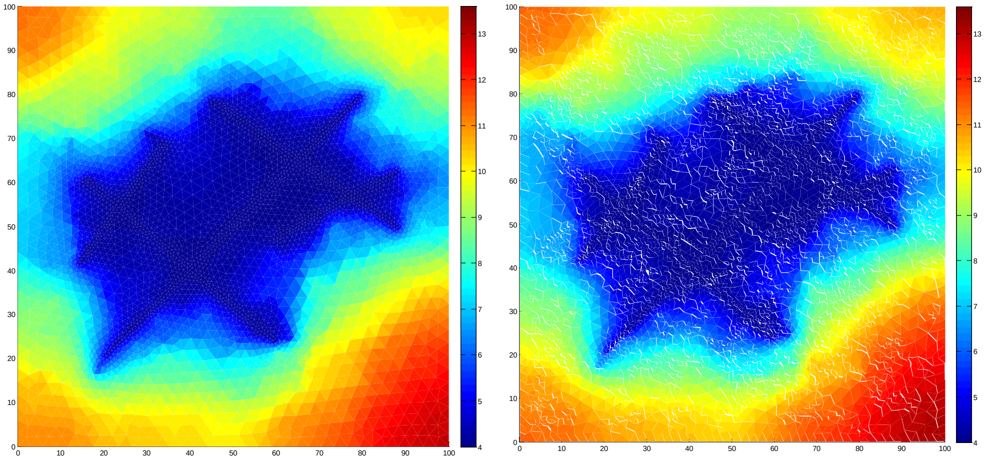

Figure 2.15: Pressure profile of the matrix at 1200day for the hybrid (9916) and reference model.

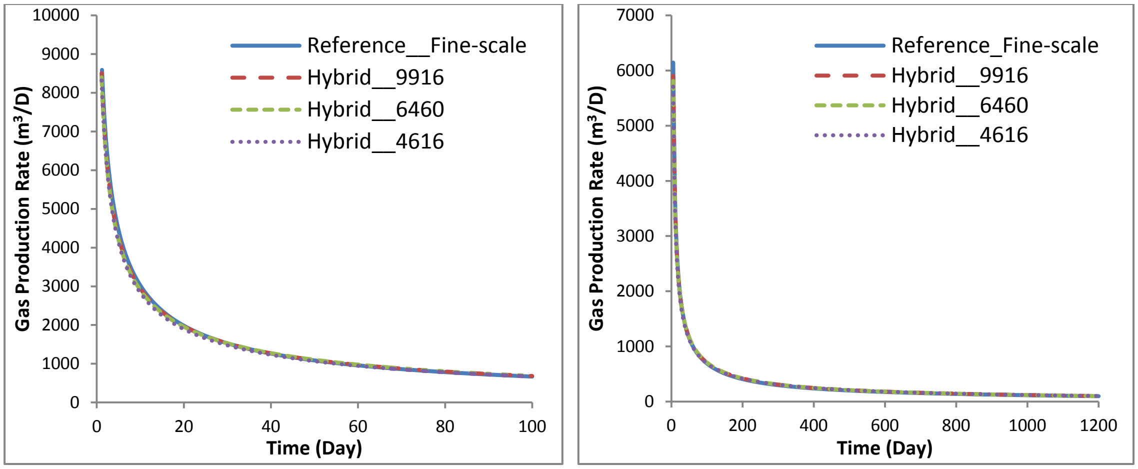

Figure 2.16: Gas rates for the first 100 and 1200 days obtained from the hybrid and reference model.

We validate the hybrid model and the associated upscaling procedure by comparison to a fine-scale DFM model where all fractures are discretized explicitly. The reference fine-scale model comprises 18239 grid blocks (matrix and fracture). A sequence of 3 hybrid grids is generated with 4616, 6460, and 9916 grid blocks respectively which correspond to refinement ratios of approximately 0.25, 0.35, and 0.55 relative to the reference grid dimension. For each of the three hybrid grids, the stochastically generated natural fractures are upscaled using our proposed procedure while the primary fractures are discretized explicitly. **Fig. 2.13** shows the finest hybrid grid and the reference grid. The fine-scale reference model results in much more gridblocks than the hybrid model due to the complex geometry of the natural fracture network, which should be honored precisely by grid refinement to maintain satisfying grid quality. All four models are run to a total simulation time of 1200 days using a constant 5 day time step size.

The pressure profiles of the matrix obtained at 600 and 1200 day using the finest hybrid grid and the reference grid appear in **Figs. 2.14/2.15**. The transient gas rates obtained from the hybrid and reference model are shown in **Fig. 2.16** for the first 100 and 1200 days. The hybrid models provide accurate solutions for both early transient and long-term production periods. We note that the natural fracture network selected for this case is relatively sparse. This choice is made due to the difficulty in generating a quality mesh for the reference model. In practice, it is anticipated that for denser fracture networks, significant gains in computational efficiency would be obtained by the use of a hybrid model compared to the reference model. The relative CPU times for the hybrid model simulations relative to the reference model are 0.21, 0.31, and 0.53 respectively.

2.4 Further simulation examples

2.4.1 Hybrid Model I: EDFM-MINC

During the development phase of an unconventional reservoir in order to determine well spacing for infill projects, multiple wells (sector modeling) may have to be incorporated into the simulation model. To demonstrate the capability and the efficiency of the EDFM-MINC hybrid model for simulating multi-well scenarios, a shale gas reservoir model with two parallel horizontal wells (well spacing: 200m) intersected by a complex network of primary fractures is established. The hydraulically activated fracture network is described by the SRV concept. The schematic of the model and the parameters modified from Table 2.6 are shown in **Fig. 2.17** and Table 2.9.

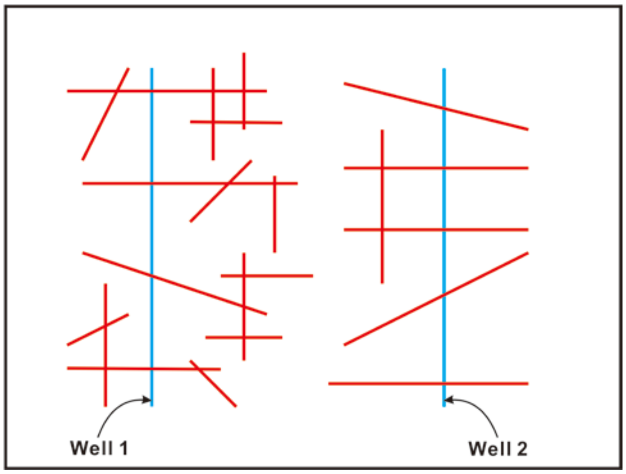

Figure 2.17: Schematic of the two-well interference model.

Table 2.9: Modified parameters for the two-well model.

Parameter	Value	Unit
Reservoir dimensions (x,y,z)	400, 300, 10	m
Gridblock size (x,y,z)	10, 10, 10	m
Matrix permeability	2.0e-20	m^2
Natural fracture permeability	1.0e-13	m^2
Rock density	2500	kg/m^3
Langmuir pressure, CH_4	4.0	MPa
Langmuir volume, CH_4	0.018	m^3/kg

2.4.1.1 Effect of MINC Refinement and Fracture Network Spacing: In order to determine the optimal number of MINC nested-cells for this simulation case, we perform sensitivity analysis for the relation between MINC refinement and fracture network spacing. The fluid system contains gas (initial water saturation set to zero), and desorption from the matrix is considered given that the steepness of the potential gradient around the fracture network will be exacerbated where desorption is present (Freeman et al. 2013). Only Well 2 is open for production in this simulation study. We compare the fracture spacing (L=10, 30, 60m), with combination of nested-cells quantity for MINC (Nm=1, 4, 7). The gas rates of Well 2 for different cases are shown in **Fig. 2.18**. From the result we could see that the dual-porosity model (Nm=1) completely misses the transient flow behavior of the ultra-tight matrix for a long period. For smaller fracture spacing case (L=10m), smaller difference of the gas rate between Nm=1 and MINC refinement is observed as expected, because the time for reaching pseudo-steady state in matrix becomes shorter. The result also shows that the differences of gas rate between Nm=4 and Nm=7 are negligible, indicating that Nm=4 level of refinement is already adequate to accurately capture the transient gas rate for this simulation scenario. In addition, fracture spacing is an influential factor for gas recovery. Smaller spacing of the fracture network could result in more effective gas drainage from matrix and gas desorption from organic rock.

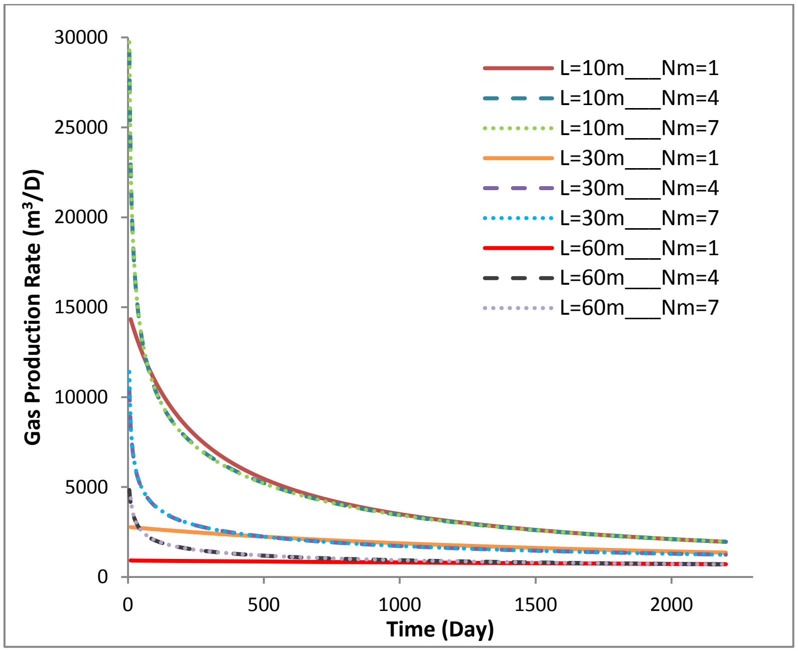

Figure 2.18: Gas rates of Well 2 for different combinations of fracture network spacing and MINC refinement.

2.4.1.2 Effect of Two-Well Interference: We perform 2-phase (gas & water) simulations for examining the effect of two-well interference. The parameters for relative permeability and capillary pressure are shown in Tables 2.7 and 2.8. The initial water saturation is set to 0.4. The number of matrix nested cells is 4, and the fracture spacing is 30m. We compare the cumulative gas production of Well 2 (right) between the cases with only Well 2, and with two wells producing on the same well schedule (shown in **Fig. 2.19**). The pressure profiles of the fracture continuum at 500/1000 day are shown in **Fig. 2.20**. From the result we could see that well interference may have a large impact on well production during the development of unconventional reservoirs, therefore multi-well scenarios should be considered for full-field simulation studies. The total simulation time is 2200 days with 5 day time step. The CPU time for the two-well case is 2.074 minutes.

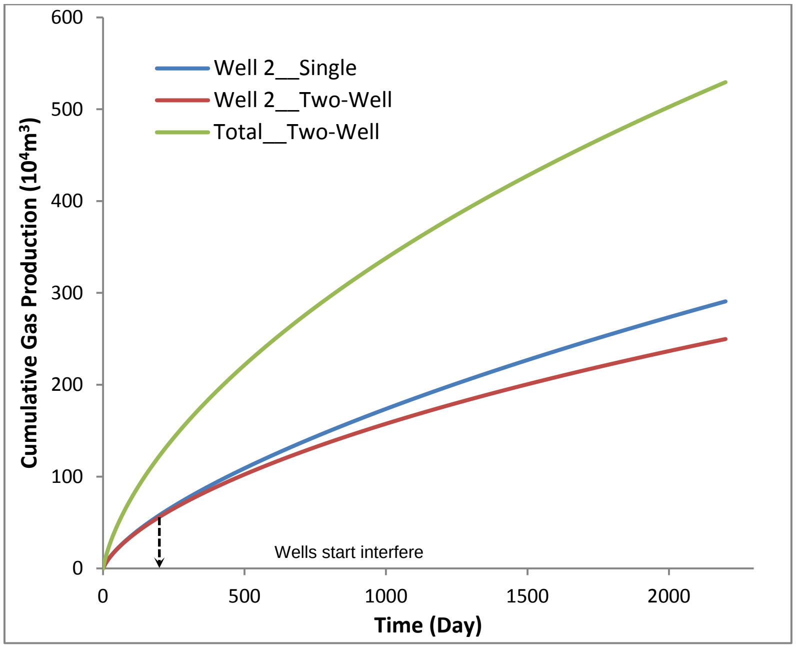

Figure 2.19: Cumulative gas production for the two-well case.

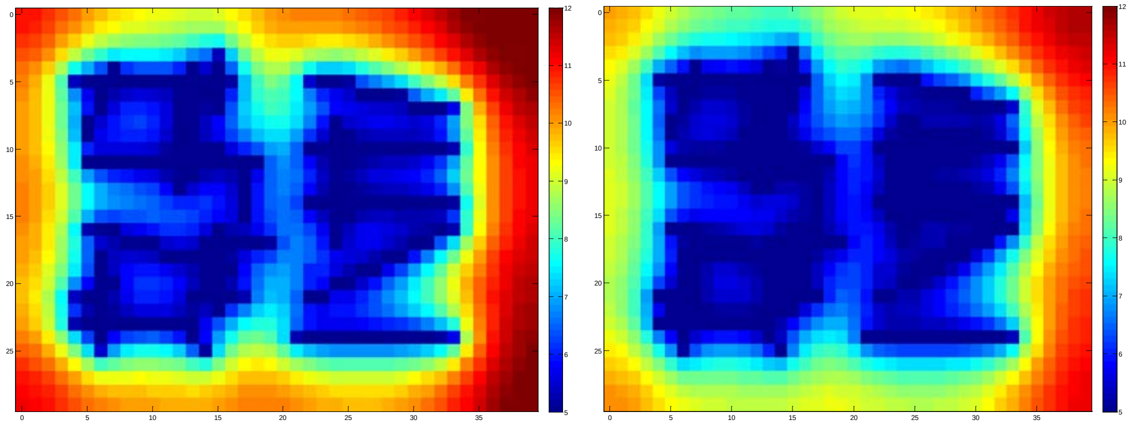

Figure 2.20: Pressure profile of the fracture continuum at 500/1000 day.

2.4.2 Hybrid Model II: UDFM-MINC

We built a reservoir model which comprises one horizontal well with three stages of hydraulic fractures to demonstrate the application of the hybrid fracture model II. We perform simulation studies to investigate the grid sensitivity and the effect of gas storage and transport mechanisms. MINC model with 4 nested-cells are applied for modeling the SRV region. Two-phase flow (gas & water) is assumed, and the parameters modified from Table 2.9 are shown in Table 2.10.

Table 2.10: Modified model parameters.

Parameter	Value	Unit
Reservoir dimensions (x,y,z)	160, 100, 10	m
Initial water saturation	0.4	
Matrix nested-cells	4	
Natural fracture spacing	30	m

2.4.2.1 Grid Sensitivity: We first perform simulations for sensitivity analysis of different grid resolution. The meshing technique used for our hybrid model yields desirable LGR feature around fracture, and produce quality meshes that are well oriented in a radial pattern around fracture tips. We run three cases with different levels of grid refinement around primary fracture (number of triangular meshes is: 2771, 4545, 7705). The mesh configuration and pressure profile of the fracture continuum at 2200 day of the three cases are shown in **Fig. 2.21**, and the log-log plot of the transient gas rates for the first 100 and 2200 days is shown in **Fig. 2.22**. As expected, minor differences in gas rate are observed among the three cases, because the conductivity contrast between primary fracture and fracture network is not so distinct. As previously mentioned, large potential gradient will not exist in the fracture network of the hybrid model (DFM+MINC), and extreme potential gradient in the matrix could be properly resolved by MINC. Therefore, relatively coarse grid refinement is already adequate to capture the transient flow behavior. The total simulation time is 2200 days with 5 day timestep. The CPU times for the three cases (2771, 4545, 7705) are 7.771, 11.999, 17.144 minutes, respectively.

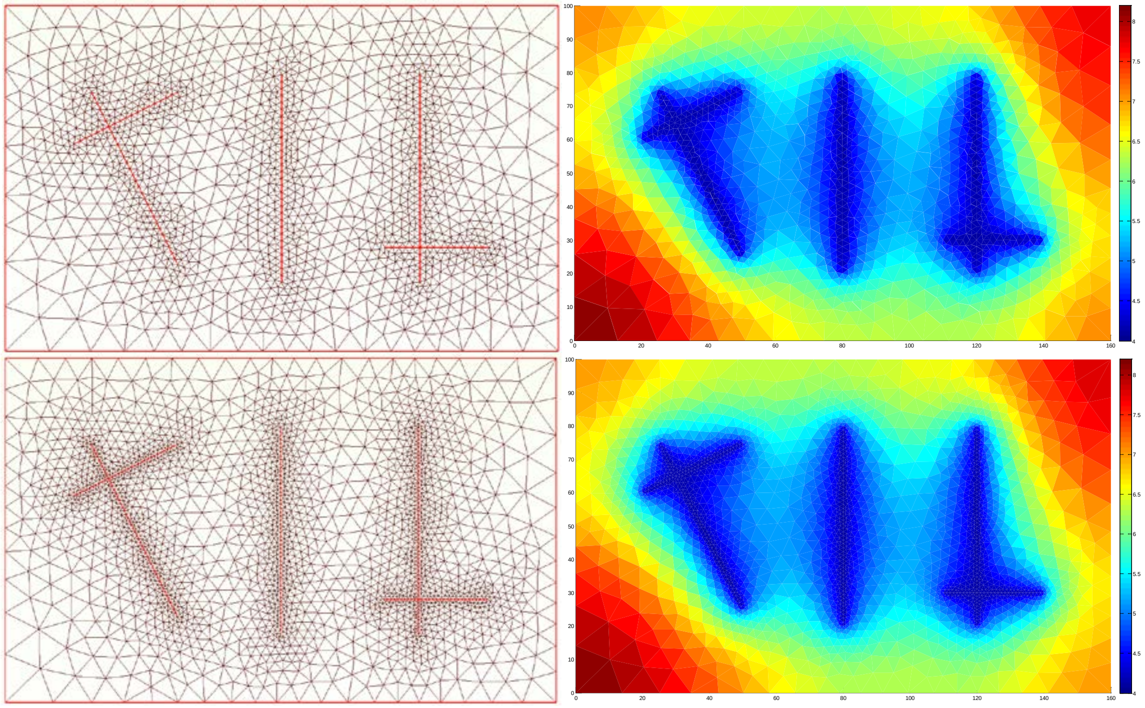

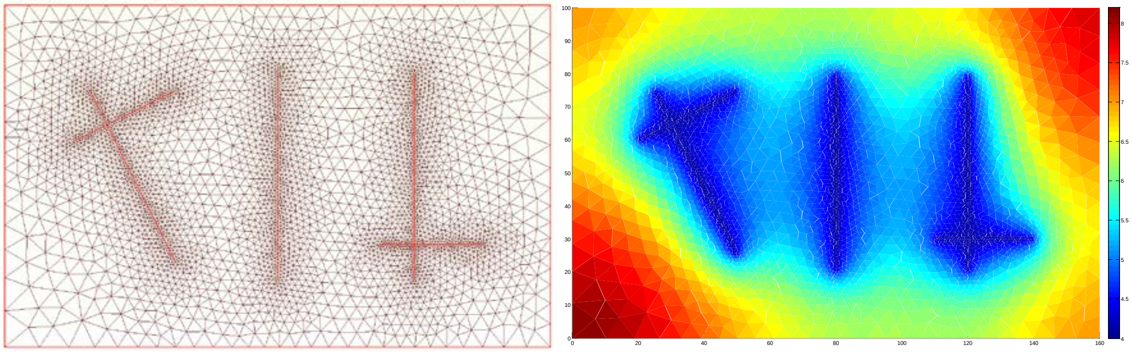

Figure 2.21: Mesh configuration and pressure profile of the fracture continuum at 2200 day of the three cases.

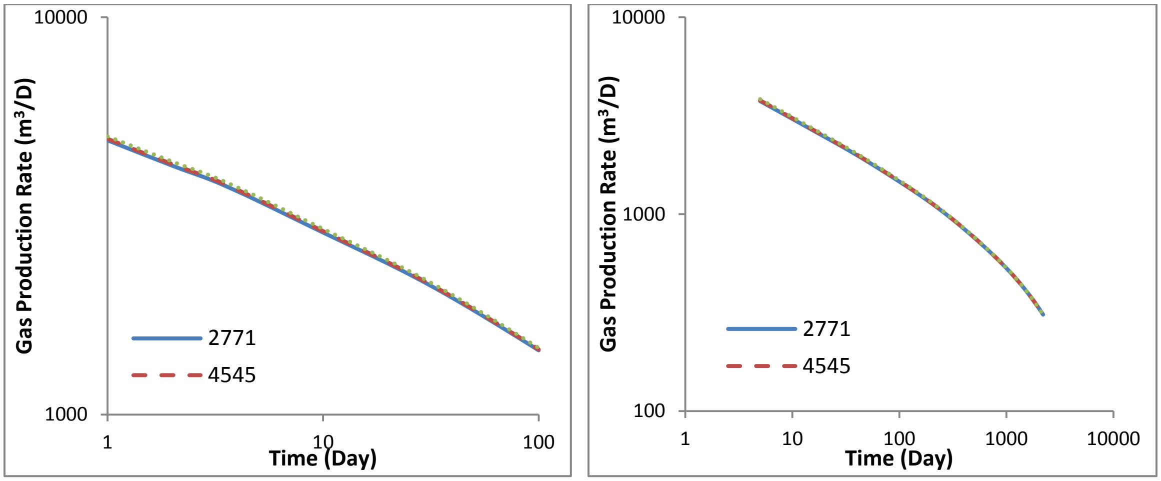

Figure 2.22: Log-Log plot for the gas rates of the three cases.

2.4.2.2 Effect of Storage and Transport Mechanism: We study the effect of storage and transport mechanism using the reservoir model with 4545 number of triangular meshes. We compare the results of 3 cases: without apparent permeability (“NoApp”), without adsorption and the base model which considers both mechanisms. **Fig. 2.23** shows the gas rate and cumulative production of the 3 cases. As can be seen, the apparent permeability correlation increases the gas production significantly. For more sparse fracture network spacing, smaller pore-throat radius and lower bottom-hole pressure, the effect of the gas transport in ultra-tight porous medium may become more significant. In addition, gas desorption also has large impact on well performance. As the reservoir pressure decreases, more adsorbed gas is released from organic rock and produced.

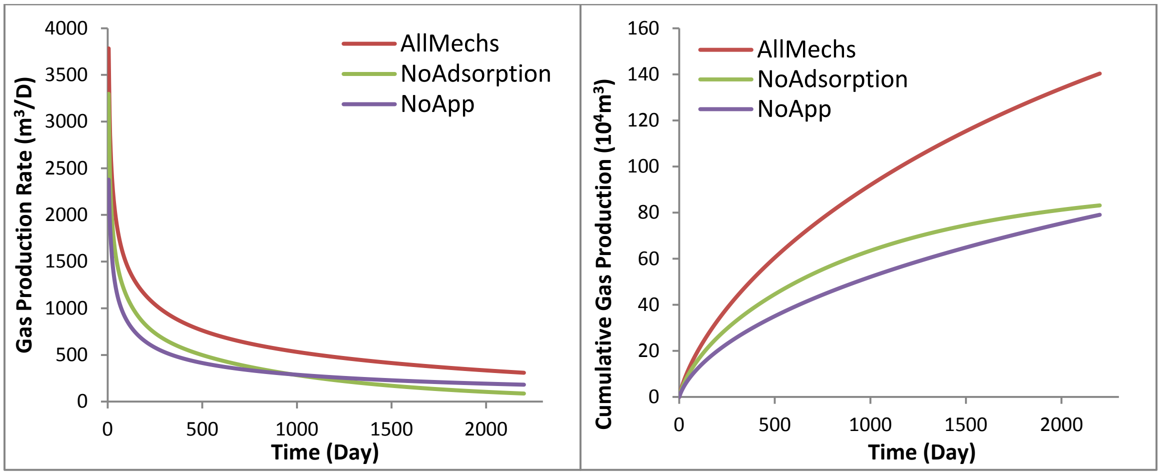

Figure 2.23: Effect of storage and transport mechanisms on gas rate/cumulative production.

2.4.2.3 Uncertainty Analysis of Multiple Realizations for Natural Fracture Network: In order to perform the uncertainty analysis of different realizations for natural fracture network, three DFN cases are stochastically generated by Monte-Carlo simulation based on the same fracture parameters (length, orientation, density, etc.) that obey log-normal distribution. The number of natural fractures for the three DFN cases is 727, 767, 599, respectively. We employ the unstructured upscaling method for the hybrid model, and we still use the reservoir model with 4545 number of triangular meshes (shown in **Fig. 2.21**). **Fig. 2.24** shows the DFN of natural fracture and the pressure profile of the matrix at 2200 day of the three cases. The cumulative gas production for the three cases and the base case without any natural fracture is plotted in **Fig. 2.25**. As can be seen, the pre-existing natural fractures have noticeable contribution on total gas production, and the regions with higher density and connectivity of natural fractures experience more effective depletion pattern. In addition, different realizations of natural fracture network may result in large difference in well performance. Such uncertainty analysis could be very useful for the model calibration during reservoir characterization. The hybrid fracture model could also be used efficiently to optimize fracture treatment and completion strategy under the uncertainty of natural fracture distribution. The total simulation time is 2200 days with 5 day timestep. The CPU times for the three DFN cases (727/767/599) and the case without any natural fracture are 3.518/3.807/3.421 and 2.296 minutes, respectively.

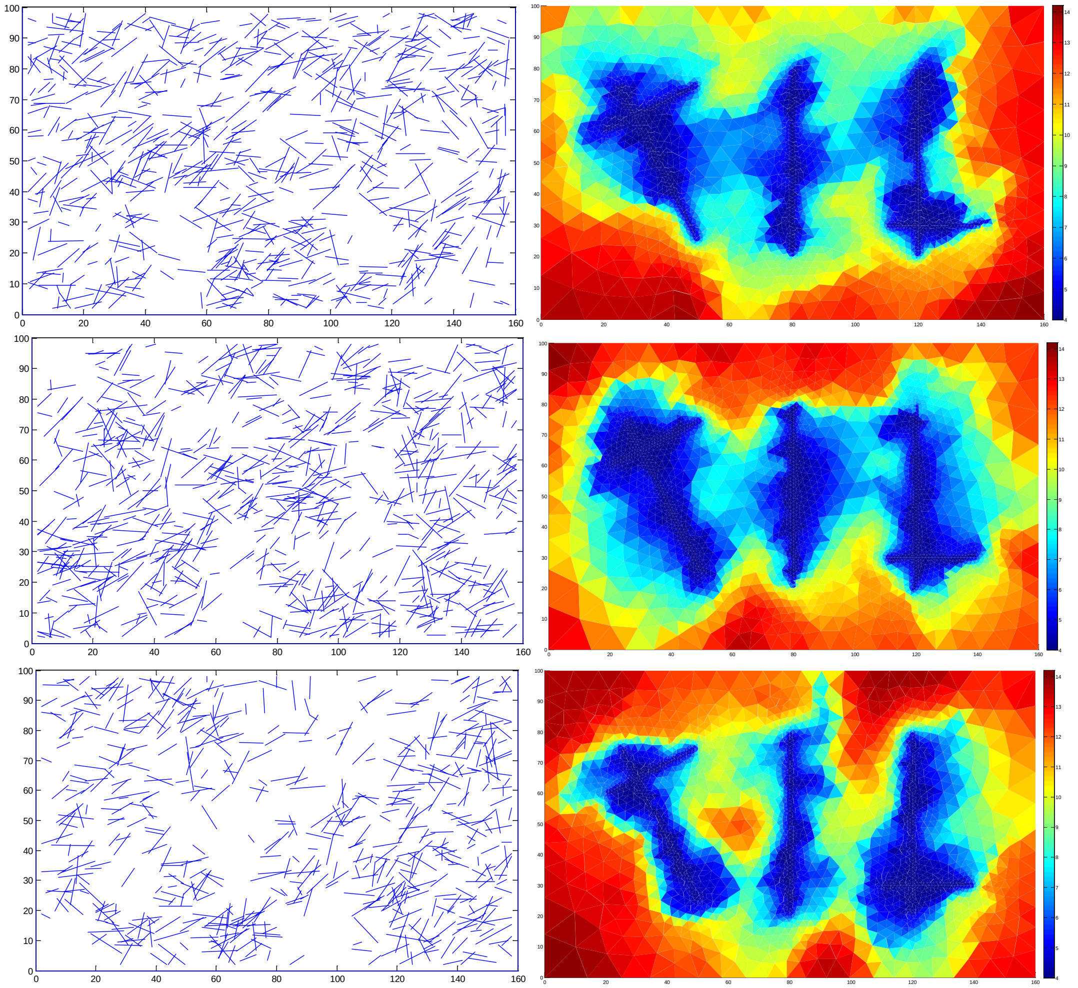

Figure 2.24: Stochastically generated DFN and pressure profile of the matrix at 2200 day of the three cases.

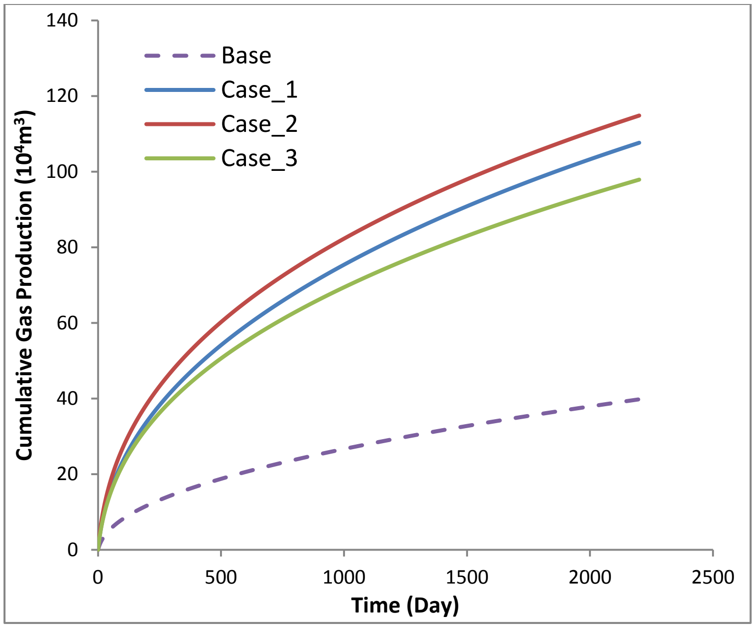

Figure 2.25: Cumulative gas production for the three cases and the base case.

CHAPTER 3

RATE TRANSIENT EFFECTS OF VARIOUS COMPLEX FRACTURE NETWORK TOPOLOGIES

In this chapter, we implement a lower-dimensional DFM model based on unstructured gridding for handling the complex fracture geometries of hydraulic fracture in stimulated formation. Optimized local grid refinement (LGR) is employed to accurately capture the transient flow regime around fractures. A consistent spatial discretization scheme called mimetic finite difference (MFD) method is applied for handling the anisotropy in matrix permeability, and the non-orthogonality of the unstructured triangular/tetrahedral grid.

We examine the effects of the irregular fracture pattern with multiple orientations on the production profile of multiple-fractured horizontal well in unconventional gas reservoir. High-fidelity numerical solutions are provided to simulate rate transient from several fracture topologies, and three-dimensional studies are performed for inclined fracture geometry. We also investigate the effects of storage and transport mechanisms in ultra-tight porous media. In addition, rate transient analysis (RTA) is performed using the theory of linear flow analysis for several simulation cases.

3.1 Numerical Model and Simulation Approach

We consider single-phase system in porous media which fills the domain $\Omega \subset \mathbb{R}^d$ (d = 2 or 3). The model assumes gas is stored in fracture as free phase, while in matrix as both free and adsorbed phase. The governing equation is the conservation of gas molar mass

$$\frac{\partial}{\partial t}\left[\phi\rho + (1-\phi)m_g\right] + \nabla \cdot \left(F_{app}\rho\boldsymbol{u}\right) = q^{fm} + q^{W} \tag{3.1}$$

we consider the gas adsorption m_g described by Langmuir isotherm in the accumulation term, and multiply apparent permeability correction F_{app} with the flux term to consider gas diffusion and slippage. q^{fm} denotes the mass communication between fracture and matrix, and it has the similar expression as flux term.

We implement the lower-dimensional DFM model in our generic, multi-continuum numerical simulator which incorporates several storage and transport mechanisms for unconventional gas reservoirs. Mimetic finite difference method is applied for discretizing the governing equations.

3.1.1 Unstructured Gridding for Complex Fracture Network

Cartesian grid system is widely applied for reservoir simulation purposes because of its simplicity. However, Cartesian grid suffers from the drawback that it cannot efficiently represent complex geologies, including non-orthogonal and non-planar fractures, and cannot adequately capture the curvilinear flow geometries expected around the fracture tips.

Although the popular Voronoi (PEBI) grid could overcome the issue of grid non-orthogonality, we use triangular/tetrahedral grid for our lower-dimensional DFM model for the reason that the current gridding technique for Voronoi grid could not properly handle fully 3D scenarios. Tetrahedral grid is more flexible than Voronoi grid, and is able to accurately capture inclined (slanted) fracture geometry.

3.1.2 Mimetic Finite Difference Method

Accurate representation of complex reservoir geology using unstructured mesh, and upscaling of high-resolution geostatistical reservoir models into full-tensor permeability fields would pose big challenge to numerical discretization techniques for reservoir simulation (Alpak 2010). Combined effects of grid non-orthogonality induced by mesh distortion and strong permeability anisotropy cannot be resolved by conventional two-point flux approximation scheme (TPFA); therefore may result in large errors in flow predictions (Aavatsmark 2002). Several consistent discretization schemes such as multi-point flux approximation (MPFA), mixed finite-element (MFE) and mimetic finite difference (MFD) method were developed to overcome these challenges. This work focuses on the MFD method for discretizing the lower-dimensional DFM model because of its generality and flexibility in handling the unstructured domains and non-planar fracture geometries. MFD exhibits some advantageous characteristics: 1) locally conservative, 2) second-order accurate for cell-center potential and first-order accurate for cell-face flux on smoothly distorted meshes with heterogeneous and fully anisotropic permeability field and 3) leads to a sparse symmetric positive definite coefficient matrix (Alpak 2010).

For simplicity, let us consider the incompressible single-phase flow equation

$$\nabla \cdot \boldsymbol{u} = q, \qquad \boldsymbol{u} = -\boldsymbol{K}\nabla p \tag{3.2}$$

a consistent, finite-volume formulation for general polygonal and polyhedral grid gives the cell-based, local discretization of Darcy's law as (Lie et al. 2012)

$$\boldsymbol{u}_i = \boldsymbol{T}_i(\boldsymbol{e}p_i - \boldsymbol{\pi}_i) \tag{3.3}$$

where $\boldsymbol{u}_i$ is a vector of all fluxes associated with a cell Ω_i, $\boldsymbol{e} = (1, \dots, 1)^T$, $\boldsymbol{\pi}_i$ is a vector of face pressures, and $\boldsymbol{T}_i$ is a matrix of one-sided transmissibilities. The local discretization is

$$\boldsymbol{M}_i\boldsymbol{u}_i = \boldsymbol{e}p_i - \boldsymbol{\pi}_i \tag{3.4}$$

where the matrix $\boldsymbol{M_i}$ is referred to as the local inner product.

In the following formulation, the continuity of fluxes across cell faces is introduced as a set of equations that together with mass conservation and Darcy's law constitute a coupled system for cell pressure, face pressure, and fluxes. By collecting the local discretization on each cell, we could derive a linear system of discrete global equations (Singh 2010)

$$\begin{bmatrix} \mathbf{B} & \mathbf{C} & \mathbf{D} \\ \mathbf{C}^{\mathrm{T}} & \mathbf{0} & \mathbf{0} \\ \mathbf{D}^{\mathrm{T}} & \mathbf{0} & \mathbf{0} \end{bmatrix} \begin{bmatrix} \boldsymbol{u} \\ -\boldsymbol{p} \\ \boldsymbol{\pi} \end{bmatrix} = \begin{bmatrix} \mathbf{0} \\ \boldsymbol{q} \\ \mathbf{0} \end{bmatrix} \tag{3.5}$$

where the first row in the block-matrix equation corresponds to Eq .4 for all grid cells. The vector $\boldsymbol{u}$ contains the outward fluxes associated with half faces ordered cell-wise, the vector $\boldsymbol{p}$ contains the cell pressures, and $\boldsymbol{\pi}$ the face pressures. The matrices $\mathbf{B}$ and $\mathbf{C}$ are block diagonal with each block corresponding to a cell. Each column of $\mathbf{D}$ corresponds to a unique interface in the grid and has two unit entries for interfaces between cells in the interior of the grid. Similarly, $\mathbf{D}$ has a single unit entry in each column that corresponds to an exterior interface.

MFD methods are constructed so that they are exact for linear pressure fields and give a symmetric positive-definite matrix $\boldsymbol{M_i}$. Consider two neighboring gridcells K and K' with interface E (that is, $E = K \cap K'$), shown in **Fig. 3.1**. Let $\boldsymbol{n}_K$ denote the area-weighted normal vector to E and $\boldsymbol{x}_K$ be the vector pointing from the centroid of cell Ω_K to the centroid of face E.

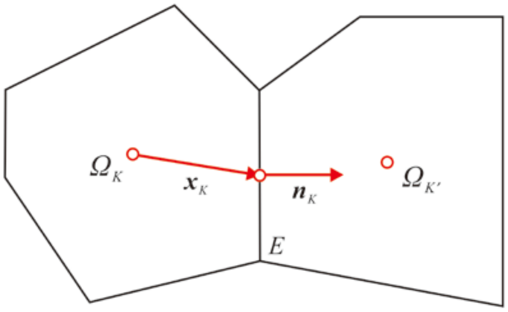

Figure 3.1: Schematic for two neighboring gridcells.

All vectors $\boldsymbol{x}_K$ and $\boldsymbol{n}_K$ defined for the cell Ω_K are collected as rows in two matrices $\boldsymbol{X}_i$ and $\boldsymbol{N}_i$. We see that the matrices $\boldsymbol{M_i}$ and $\boldsymbol{T_i}$ must satisfy the following consistency conditions (Brezzi et al. 2005)

$$\boldsymbol{MNK} = \boldsymbol{X}, \quad \boldsymbol{NK} = \boldsymbol{TX} \tag{3.6}$$

how to obtain a symmetric positive-definite matrix $\boldsymbol{M_i}$ is the key step for the MFD method. A strict theorem is presented by Brezzi et al. (2005), where they give a recipe for constructing $\boldsymbol{M_i}$. The symmetric and positive definite inner product that fulfills Eq. 3.6 can be represented in the compact form

$$\begin{aligned} \boldsymbol{M} &= \frac{1}{|\Omega_i|}\boldsymbol{XK}^{-1}\boldsymbol{X}^{\mathrm{T}} + \boldsymbol{Q}_N^{\perp}\boldsymbol{S}_M\boldsymbol{Q}_N^{\perp\,\mathrm{T}} \\ &= \frac{1}{|\Omega_i|}\boldsymbol{XK}^{-1}\boldsymbol{X}^{\mathrm{T}} + \boldsymbol{P}_N^{\perp}\boldsymbol{S}_M\boldsymbol{P}_N^{\perp} \end{aligned} \tag{3.7}$$

where $\boldsymbol{S}_M$ denotes any symmetric, positive definite matrix, $\boldsymbol{Q}_N^{\perp}$ is an orthonormal basis for the left null space of $\boldsymbol{N}^{\mathrm{T}}$, and $\boldsymbol{P}_N^{\perp}$ is the null-space projection $\boldsymbol{I}-\boldsymbol{Q_N}\boldsymbol{Q_N}^{\mathrm{T}}$ in which $\boldsymbol{Q_N}$ is a basis for the spaces spanned by the columns of $\boldsymbol{N}$.

Similarly, we can derive a closed expression for the inverse inner product $\boldsymbol{T}$

$$\begin{aligned}\boldsymbol{T} &= \frac{1}{|\Omega_i|}\boldsymbol{NKN}^{\mathrm{T}} + \boldsymbol{Q}_X^{\perp}\boldsymbol{S}_T\boldsymbol{Q}_X^{\perp\mathrm{T}} \\ &= \frac{1}{|\Omega_i|}\boldsymbol{NKN}^{\mathrm{T}} + \boldsymbol{P}_X^{\perp}\boldsymbol{S}_T\boldsymbol{P}_X^{\perp}\end{aligned} \tag{3.8}$$

where $\boldsymbol{Q}_X^{\perp}$ is an orthonormal basis for the left nullspace of $\boldsymbol{X}^{\mathrm{T}}$ and $\boldsymbol{P}_X^{\perp}=\boldsymbol{I}-\boldsymbol{Q_X}\boldsymbol{Q_X}^{\mathrm{T}}$ is the corresponding nullspace projection.

In this work, the following inverse inner product has been used (Singh 2010)

$$\boldsymbol{T}=\frac{1}{|\Omega_i|}\left[\boldsymbol{NKN}^{\mathrm{T}}+\frac{6}{d}\operatorname{trace}(\boldsymbol{K})\boldsymbol{A}(\boldsymbol{I}-\boldsymbol{QQ}^{\mathrm{T}})\boldsymbol{A}\right] \tag{3.9}$$

where $\boldsymbol{A}$ is the diagonal matrix containing face areas and $\boldsymbol{Q}=\operatorname{orth}(\boldsymbol{AX})$, d the space dimension, and $\boldsymbol{I}$ the identity matrix.

For the conventional TPFA scheme, the resulting $\boldsymbol{T}_i$ matrix is diagonal, and the one-sided transmissibility for gridcell K sharing interface E is

$$T=\boldsymbol{n}\cdot\boldsymbol{Kx}/|\boldsymbol{x}|^2 \tag{3.10}$$

in the two-point method, the linear system is developed by combining mass conservation and Darcy’s law into one second-order discrete equation for the pressure. Then the total face transmissibility that combines two half-transmissibilities in a harmonic average for two neighboring cells could be calculated.

3.1.3 Lower-Dimensional DFM Discretization

The reservoir and fracture are modeled in two separate domains in this work. The reservoir model is set in $\Omega \subset \mathbb{R}^d$ (d = 2 or 3). Since fractures have an order of magnitude smaller length scale (fracture width) compared to reservoir, the boundary is represented as a lower dimensional surface in $\mathbb{R}^{d-1}$. We apply the method called fracture cross flow equilibrium (FCFE) which is introduced by Hoteit and Firoozabadi (2008) to determine the boundary condition for fracture and matrix communication. The pressure is assumed to be equal along the fracture width, and thus only the degree of freedom for fracture cell pressure is remained at the fracture-matrix interface. The schematic for FCFE concept is shown in **Fig. 3.2**.

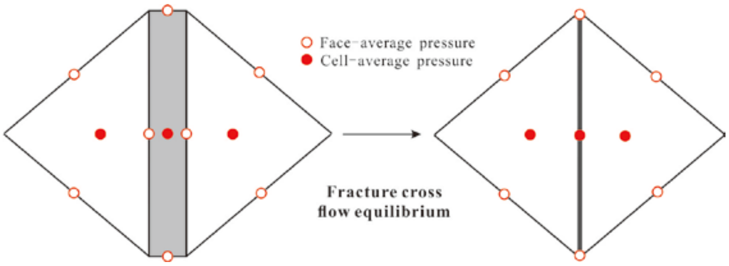

Figure 3.2: Schematic of FCFE concept for treating fracture-matrix interface (modified from Hoteit and Firoozabadi 2008).

As previously mentioned, in mimetic finite difference method the flux is written locally for all faces within each gridcell. To assemble all the gridcells together, the following continuity conditions for the flux and the pressure are imposed at each interface E of two neighboring matrix gridcells K and K' ($E = K \cap K'$). We use $q_{K,E}^{m}$ for the gas mass flux in the following discussions.

If E is neither a fracture nor a barrier, the continuity of flux and pressure is imposed

$$\begin{cases} q_{K,E}^{m} + q_{K',E}^{m} = 0 \\ \pi_{K,E}^{m} = \pi_{K',E}^{m} \end{cases} \tag{3.11}$$

If E is a fracture, the total flux across both sides of the matrix-fracture interface defines the transfer function Q_E^f at E, which acts as a sink/source term. The continuity of the pressure across the fracture-matrix interface E is imposed

$$\begin{cases} q_{K,E}^{m} + q_{K',E}^{m} = Q_E^f \\ \pi_{K,E}^{m} = \pi_{K',E}^{m} = p_E^f \end{cases} \tag{3.12}$$

In addition to the above conditions, the flux and pressure at the domain boundaries are described by the Neumann or Dirichlet boundary conditions. If the interface E is at the domain's boundary, then

$$\begin{cases} q_{K,E}^{m} = q_E^N \\ \pi_{K,E}^{m} = \pi_E^D \end{cases} \tag{3.13}$$

where π_E^D is a Dirichlet boundary condition, and q_E^N is a Neumann boundary condition. In this work, we assume an impermeable boundary and set $q_{K,E}^m$ to be zero at the boundary.

The linear system as in Eq. 3.5 may also be derived for the fracture domain, and from Eq. 3.11/3.12/3.13, we can eliminate the flux variables and construct a system consisting of the unknowns for cell pressure and face pressure. For the discretization of the compressible real-gas flow described by Eq. 3.1, the system will become nonlinear and can be solved by Newton's method.

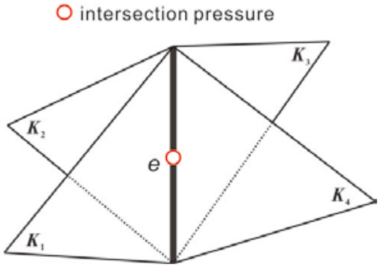

Figure 3.3: Schematic for fracture intersection.

For fracture-fracture intersection e, we assume that the interface has a negligible volume, and thus no mass accumulation is considered. Similar continuity conditions as in Eq. 3.11 is imposed at e. The schematic for fracture intersection is shown in **Fig. 3.3**.

$$\begin{cases} \sum_{i=1}^{n_e} q_{K_i,e}^{f} = 0 \\ \pi_{K_i,e}^{f} = p_e^{f} \end{cases} \tag{3.14}$$

where n_e is the number of fracture cells that connect to the intersection e and p_e^f is the fracture intersection pressure.

3.2 Simulation Results and Discussions

We build a base model which comprises one horizontal well with five stages of hydraulic fractures to demonstrate the application of the developed DFM model. The base model parameters are summarized in Table 3.1. The hydraulic fractures are assumed to fully penetrate the formation. Gas desorption and the apparent permeability for gas transport mechanism are considered. We assume that the well is located in a drainage region that extends beyond the fracture tips, and the flow contribution from outside of this region is negligible. We set impermeable boundaries at the outer limits of our drainage region.

We run simulation studies to demonstrate the applicability of our lower-dimensional DFM model. We examine the effects of the irregular fracture pattern with complex geometries on the transient gas rate of multiple-fractured horizontal wells.

Table 3.1: Base model parameters.

Parameter	Value	Unit
Reservoir dimensions (x,y,z)	200, 140, 10	m
Initial reservoir pressure	16	MPa
Temperature	343.15	K
Matrix porosity	0.1	
Fracture porosity	1.0	
Intrinsic matrix permeability	1.0e-19	m^2
Rock density	2500	kg/m^3
Langmuir pressure, CH_4	4.0	MPa
Langmuir volume, CH_4	0.018	m^3/kg
Matrix compressibility	1.0e-9	1/Pa
Fracture compressibility	1.0e-8	1/Pa
Fracture width	1.0e-3	m
Fracture permeability	1.0e-12	m^2
Fracture spacing	25	m
Fracture half-length	30	m
Well radius	0.1	m
Producer BHP	4	MPa
Production time	2500	day

3.2.1 Effect of Storage and Transport Mechanisms

High-resolution is needed near fracture to capture the large pressure gradient and the corresponding changes of the gas compressibility and viscosity in the ultra-tight matrix. The meshing technique used for the DFM model yields desirable local grid refinement (LGR) feature around fracture, and produce quality meshes that are well oriented in a radial pattern around fracture tips. The LGR feature ensures that the evolution of flow regimes is accurately represented.

We study the effect of storage and transport mechanism using the reservoir model with 10334 number of triangular meshes. We compare the results of 4 cases: without apparent permeability (“NoApp”), without adsorption, the base model which considers both mechanisms (“AllMechs”) and does not consider any mechanism (“NoMechs”). The mesh configuration and the pressure profile in the reservoir at 2500 day for the "AllMechs" case are shown in **Fig. 3.4**, and the log-log plot of the gas rates for the 4 cases is shown in **Fig. 3.5**. From the gas-rate curve of the "NoMechs" case, 4 different flow regimes that are expected in a multiple-fractured horizontal well (MFHW) system could be identified:

1. Fracture linear flow (flow regime I, 1e-4 day to 1e-2 days): hydraulic fractures start flowing to the horizontal wellbore;
2. Transition flow (flow regime II, 1e-2 day to 1 days): the transition from fracture bilinear flow to formation linear flow;
3. Formation linear flow (flow regime III, 1 day to 1000 days): formation linear flow which is perpendicular to the fracture faces, with half slope in log-log plot; the dominant flow regime for a typical MFHW in unconventional gas reservoir;
4. Compound-linear flow (flow regime IV, after 1000 days): hydraulic fractures begin to interfere, which results in the deviation from the half slope, and may appear like boundary-dominated flow.

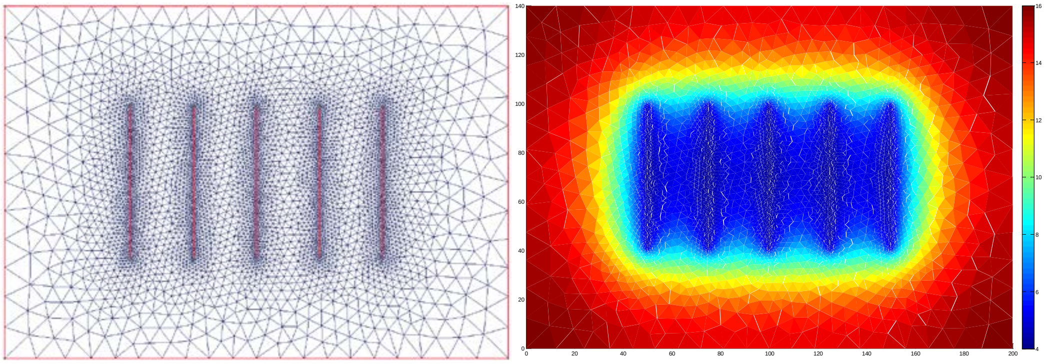

Figure 3.4: Mesh configuration and pressure profile at 2500 day of the "AllMechs" case.

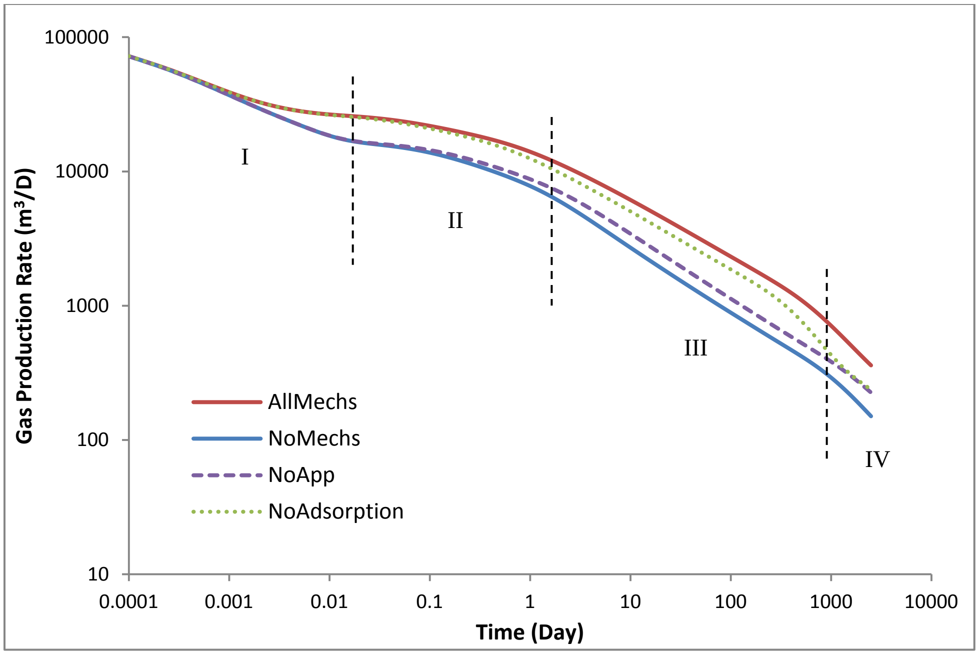

Figure 3.5: Effect of storage and transport mechanisms on gas rate.

From the results we could see that apparent permeability increases the gas production significantly. The gas slippage and Knudsen diffusion tend to have larger effect when the pressure becomes lower during late time depletion. For smaller pore-throat radius and lower bottom-hole pressure, the effect of the gas transport in ultra-tight porous medium may become more significant.

In addition, gas desorption also has large impact on well performance. As the reservoir pressure decreases, more adsorbed gas is released from organic rock and produced. However, for some moderate to deep shale-gas reservoirs which have high initial pressure, the ability to produce the adsorbed gas may be very limited because of the Langmuir sorption profile, which requires relatively low pressure to expedite the desorption process.

3.2.2 Comparison Between TPFA and MFD scheme

Grid non-orthogonality and strong permeability anisotropy may introduce large error in flow prediction if conventional two-point flux approximation scheme (TPFA) is applied. In this work, a lower-dimensional DFM model is developed based on a consistent discretization method called mimetic finite difference (MFD). We run three simulation cases with isotropic, diagonal and full-tensor permeability field in matrix for comparing between TPFA and MFD scheme. We assume that the full-tensor permeability is resulted from the upscaling of fine-scale geological model or detailed discrete fracture network model for small-scale/natural fracture.

The diagonal permeability tensor is $\boldsymbol{K} = \begin{bmatrix} \mathrm{k}_m & \\ & 0.1\mathrm{k}_m \end{bmatrix}$, and the full-tensor permeability is $\boldsymbol{K} = \begin{bmatrix} \mathrm{k}_m & 0.2\mathrm{k}_m \\ 0.2\mathrm{k}_m & 0.5\mathrm{k}_m \end{bmatrix}$, where $\mathrm{k}_m = 1.0\text{e-}19\ m^2$.

The pressure profile of the reservoir at 2500 day for the two cases with diagonal and full-tensor permeability field are shown in **Figs. 3.6/3.7**, respectively. The log-log plots of the transient gas rates for the three cases are shown in **Figs. 3.8/3.9/3.10**. For the case with isotropic permeability, the difference of gas rate between TPFA and MFD is only observed in the transition flow regime. For the other two cases, larger discrepancies are observed between the two methods. As can be seen in the pressure profiles, the lack of consistency in the TPFA scheme for handling anisotropy leads to significant grid-orientation effect. Generally speaking, errors in the solution will appear in varying degree depending upon the angles the cell faces make with the principal directions of the permeability tensor. Therefore, consistent discretization schemes such as MFD should be used for anisotropic model to provide accurate solutions.

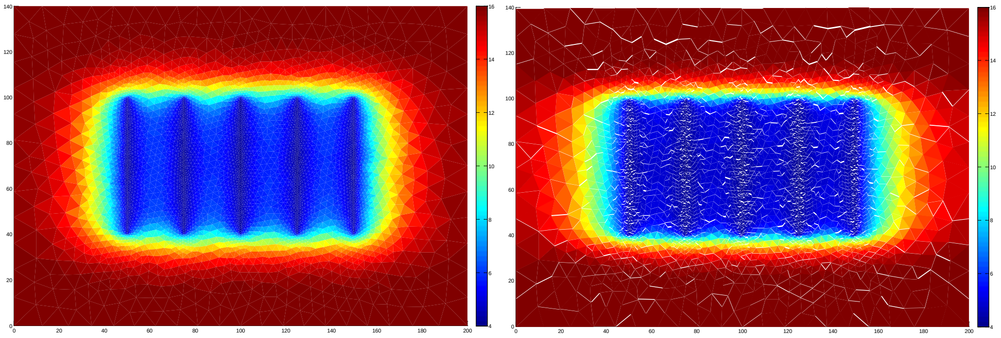

Figure 3.6: Pressure profile at 2500 day of TPFA and MFD for the diagonal permeability.

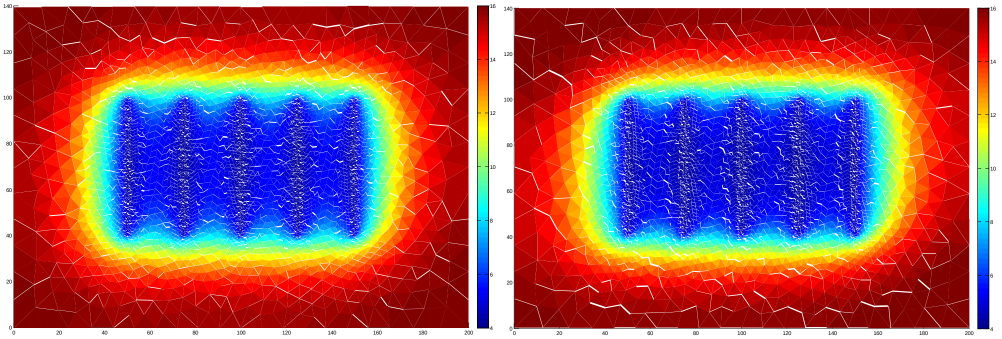

Figure 3.7: Pressure profile at 2500 day of TPFA and MFD for the full-tensor permeability.

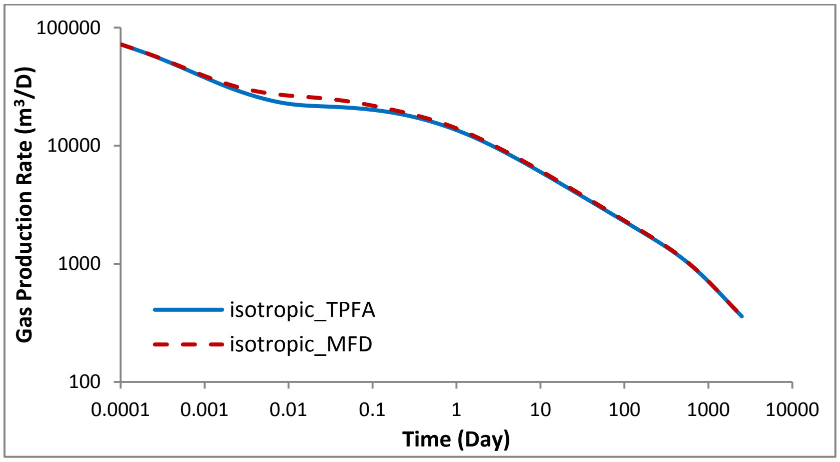

Figure 3.8: Log-Log plot for the gas rates of the case with isotropic permeability.

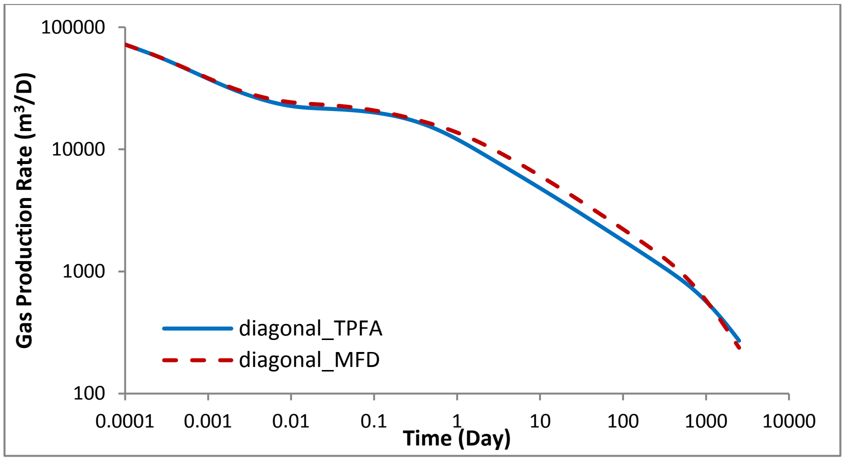

Figure 3.9: Log-Log plot for the gas rates of the case with diagonal permeability.

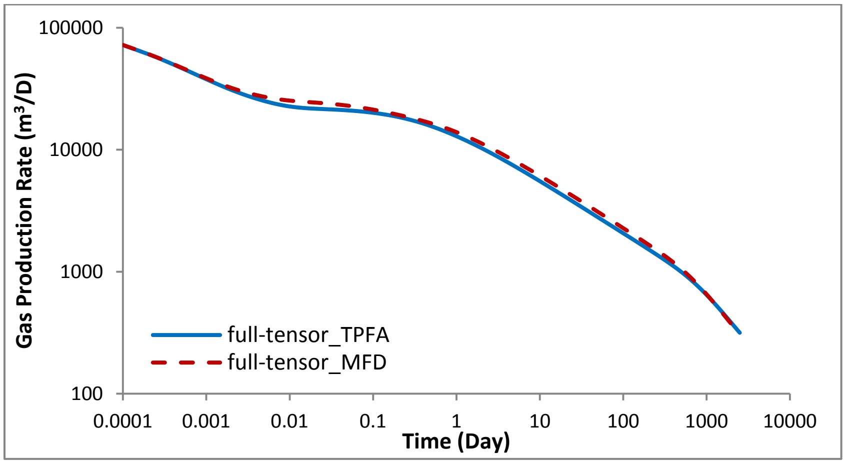

Figure 3.10: Log-Log plot for the gas rates of the case with full-tensor permeability.

3.2.3 Effect of Non-Orthogonal Fracture Geometry

Multiple-fractured horizontal wells are ideally drilled along the minimum stress direction. However, in many cases operators cannot drill in the ideal direction, and this results in the development of non-orthogonal hydraulic fracture. The hydraulic fracture planes may intersect the wellbore at an angle less than 90 degrees. We run 4 cases with the same fracture half-length and different fracture angularities (90, 60, 45, 30 degrees), to investigate the impact of non-orthogonal fracture geometry on gas rate. The intrinsic matrix permeability is reset to 4.0e-19 m^2, and the other parameters shown in Table.1 remain unchanged. For all the simulation studies regarding the fracture geometries that are presented in the paper, gas desorption and the apparent permeability for gas transport are neglected. The mesh configuration and the pressure profile of the reservoir at 2000 day for the three cases with non-orthogonal fracture geometry are shown in **Fig. 3.12**, and the log-log plot of the gas rates is shown in **Fig. 3.11**.

From the results we could observe that the gas-rate profiles for the 4 cases are almost identical during the early period. The gas rates of the cases with non-orthogonal fracture geometry gradually deviate from the orthogonal case after the occurrence of fracture interference, and the case with smaller fracture angularity exhibits fracture interference earlier. The non-orthogonal fracture systems also have lower production than the orthogonal case with the same fracture half-length, due to the reduced stimulated reservoir area within the hydraulic fractures. The results indicate that fractures should be designed so that their orientation with respect to the horizontal well should be as close to 90 degrees as possible.

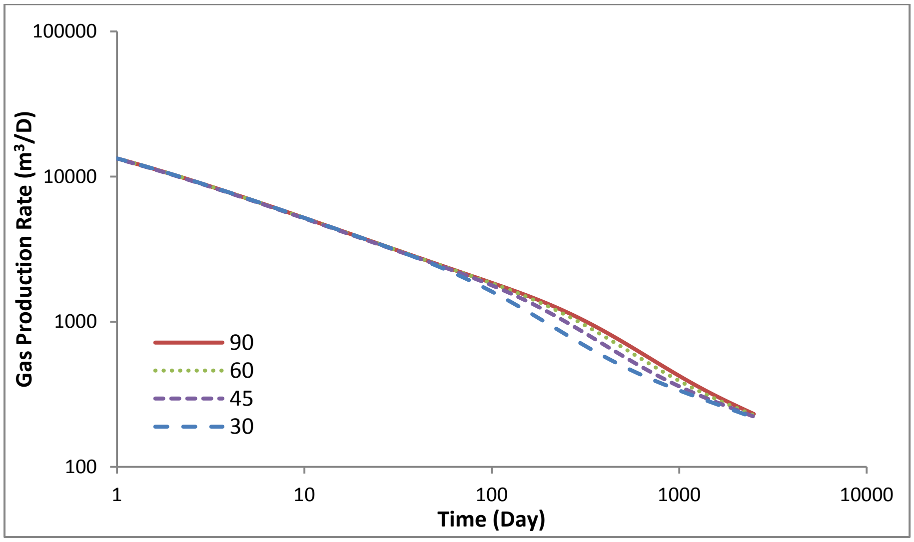

Figure 3.11: Log-Log plot for the gas rates of the four cases.

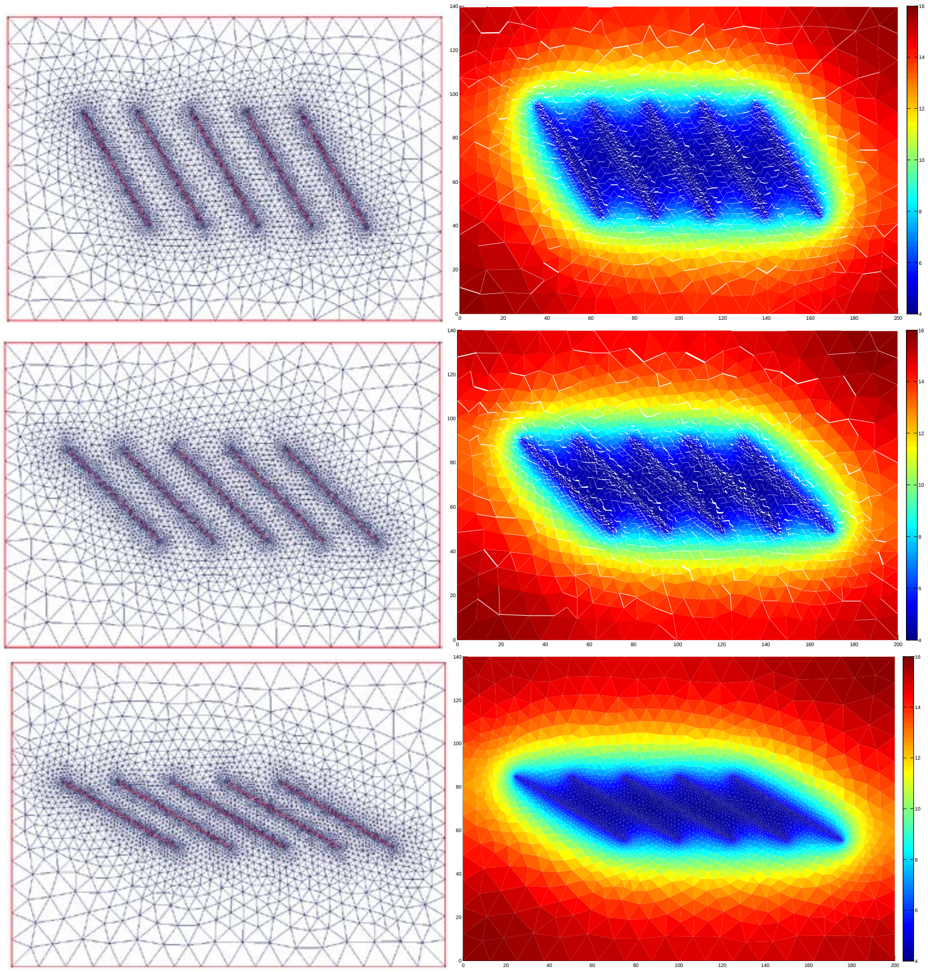

Figure 3.12: Mesh configuration and pressure profile at 2000 day of the three cases with non-orthogonal fracture geometry.

3.2.4 Effect of Non-Planar Fracture Geometry

Fracture network growth pattern could be affected by the mechanical interaction among the adjacent fractures, generally known as the “stress shadow” effect. This effect may result in significant shearing displacements along the fracture surface that will cause the fracture growth to follow a curved path (Xu and Wong 2013). The effect of stress shadowing on fracture geometry for two cases with different fracture spacing is illustrated in **Fig. 3.13** (Weng et al. 2014). As can be seen in the figure, the “stress shadow" effect may result in smaller fracture length for the inner fractures and non-planar fracture geometry. We run two cases with non-planar fracture geometry and compare the results with the regular fracture configuration. The intrinsic matrix permeability is reset to 1.0e-19m^2, and the fracture total lengths are the same for the three cases. The mesh configuration and the pressure profile of the reservoir at 2500 day of the two cases with non-planar fracture geometry are shown in **Fig. 3.14**, and the log-log plot of the transient gas rates is shown in **Fig. 3.15**.

Small differences in the gas rates between regular and non-planar fracture geometry are observed, mainly because the fracture total lengths are the same for the three cases. The small discrepancies could be induced by the complex flow pattern that exhibits near the intersection points of the fracture and the horizontal wellbore. The results show that the non-planar fracture geometry has little impact on gas rate for this simulation scenario. For more complicated fracture configuration, the effect of non-planar geometry on fracture spacing and intersection may need to be considered.

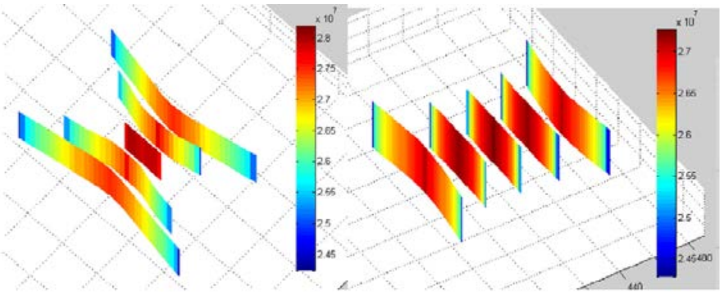

Figure 3.13: Fracture geometry induced by the effect of stress shadowing for two cases with different fracture spacing.

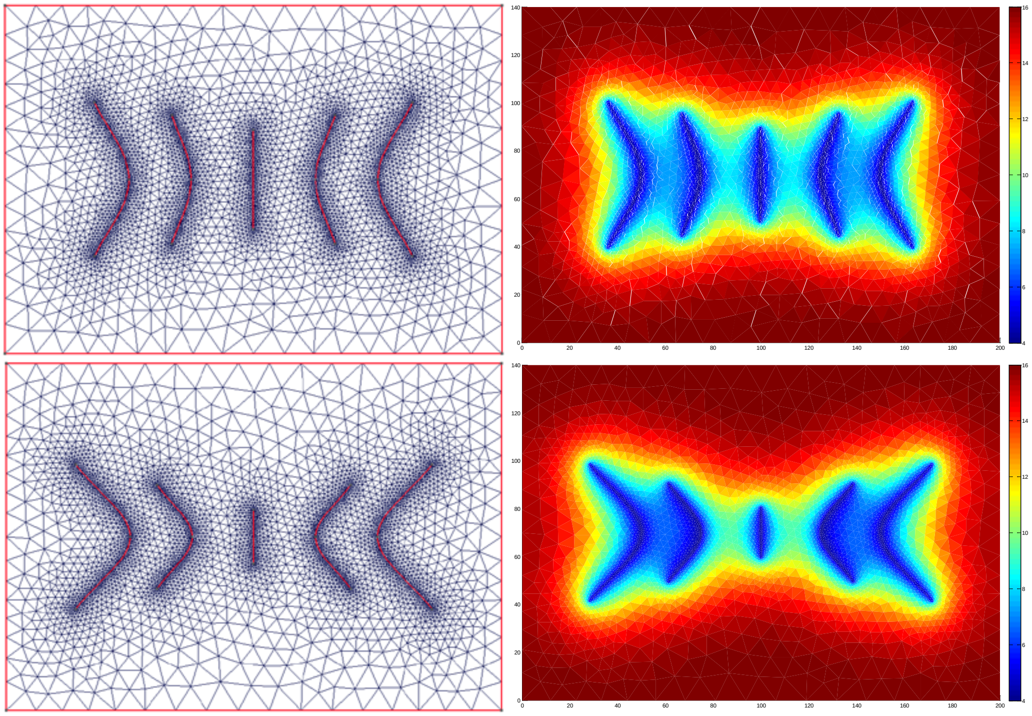

Figure 3.14: Mesh configuration and pressure profile at 2500 day of the two cases with non-planar fracture geometry.

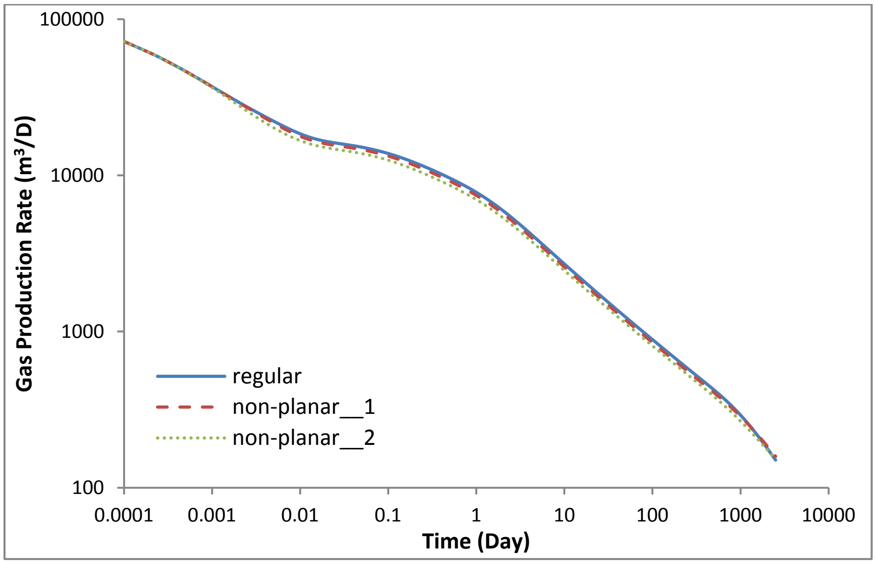

Figure 3.15: Log-Log plot for the gas rates of the three cases.

3.2.5 Effect of Inclined Fracture Geometry

For the same reason as we discuss in the "effect of non-orthogonal fracture geometry" section, the hydraulic fracture planes may also be inclined (slanted) from the vertical direction. We run 3-D simulation studies for 4 cases with different fracture inclination angles to the horizontal plane (90, 60, 45, 30 degrees), to investigate the impact of inclined fracture geometry on gas rate. The sizes of the fracture planes are the same for all cases. The parameters modified from Table 3.1 (the others remain unchanged) are shown in Table 3.2. The mesh configuration of the model that contains 3 hydraulic fractures is shown in **Fig. 3.16**, and the log-log plot of the transient gas rates is shown in **Fig. 3.17**. Optimized local grid refinement is still employed to capture the large pressure gradient around the fracture plane.

Table 3.2: Model parameters.

Parameter	Value	Unit
Reservoir dimensions (x,y,z)	200, 100, 10	m
Intrinsic matrix permeability	4.0e-19	m^2
Fracture spacing	50	m
Fracture half-length	20	m
Fracture height	10	m

From the result we could see that the gas-rate profiles for the 4 cases are almost identical during the early period. The discrepancies in gas rate are observed during the formation linear flow regime. The inclined fracture systems have higher production than the vertical case (90 degrees), simply because the reservoir volume connecting to the top and bottom boundaries of the fracture plane for the inclined fracture is larger than the vertical fracture (fracture fully penerates the formation). The result indicates that hydraulic fracture should be designed to penetrate as large formation volume as possible for maximizing well performance.

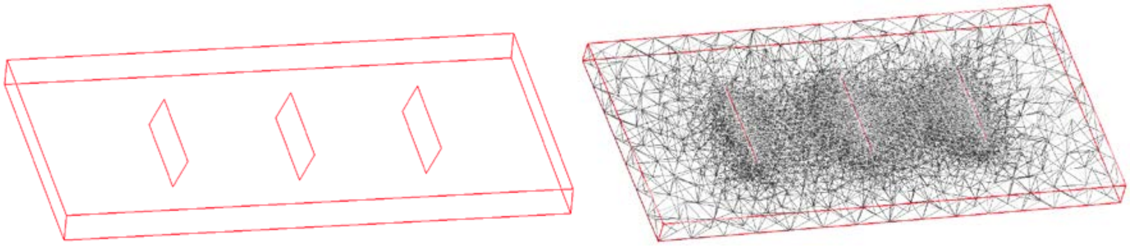

Figure 3.16: Mesh configuration of the model that contains 3 hydraulic fractures.

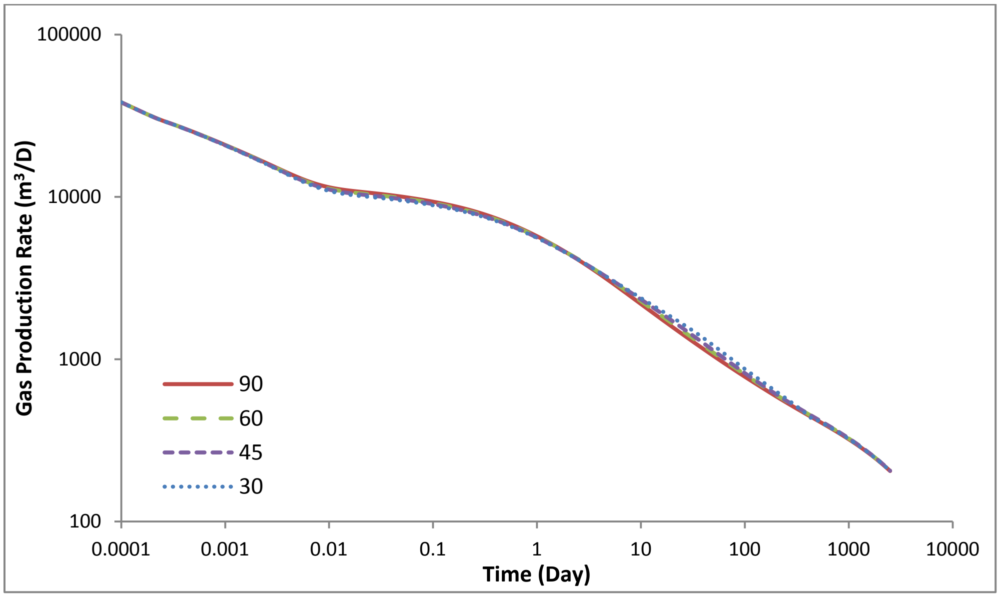

Figure 3.17: Log-Log plot for the gas rates of the four cases.

3.2.6 Effect of the Stimulated Fracture Network with Secondary Fractures

Microseismic measurements and other evidence suggest that the creation of complex fracture networks during fracturing treatment may be a common occurrence in unconventional reservoirs. Complexity is frequently associated with the interaction of hydraulic fractures with pre-existing natural fractures. Moreover, small-scale secondary fracture may be induced in the stimulated region near primary hydraulic fracture. The complex fracture network connects a huge reservoir surface area, and thus could greatly improve the well performance.

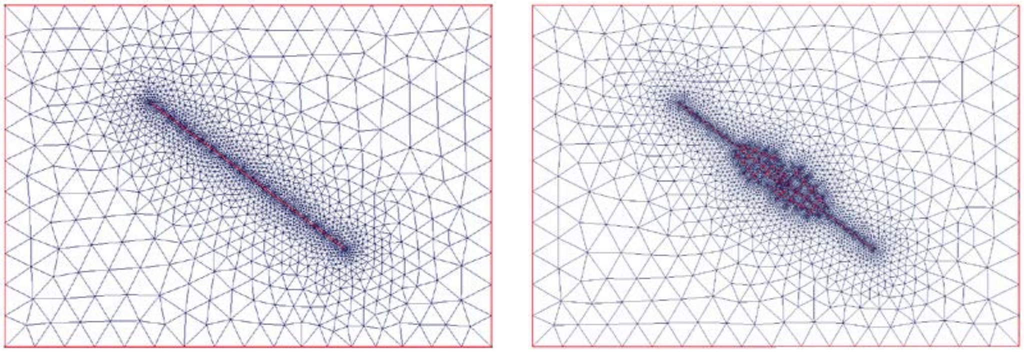

Figure 3.18: Mesh configuration of the regular and complex cases.

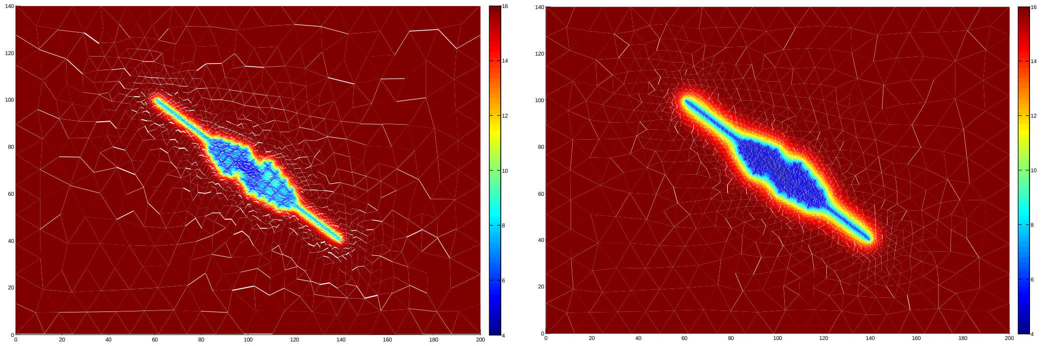

Figure 3.19: Pressure profile at 50/200 day for the complex case with the secondary fracture network.

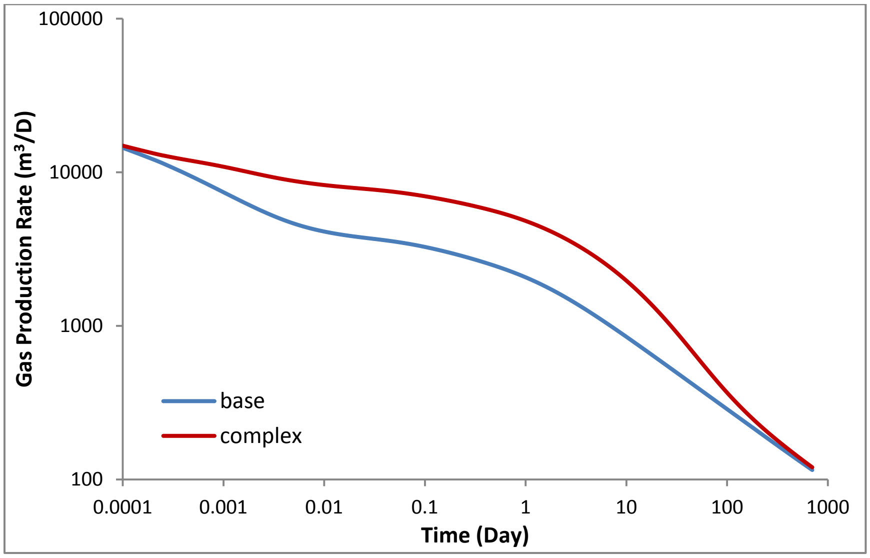

Figure 3.20: Log-Log plot for the gas rates of the two cases.

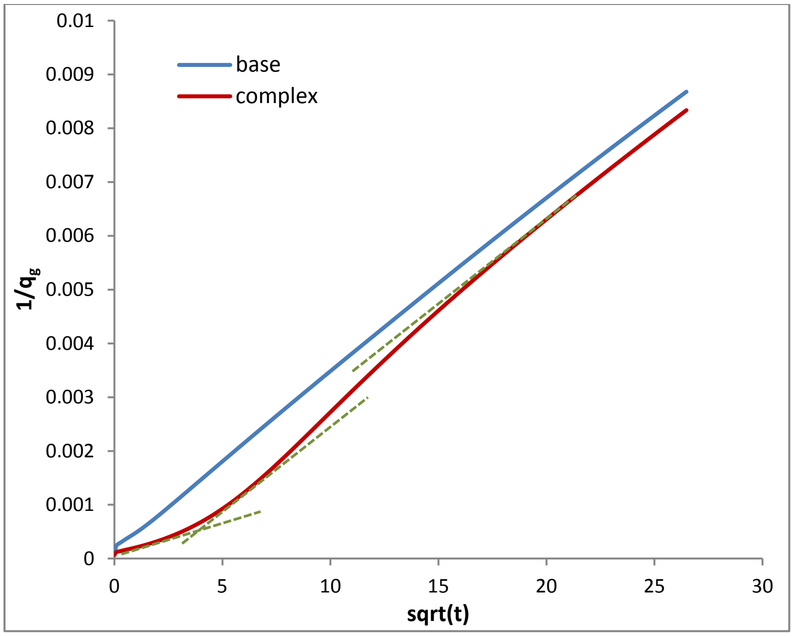

Figure 3.21: The plot of inverse gas rate vs. $\sqrt{\mathrm{t}}$ for the two cases.

We consider the model that only contains one stage of hydraulic fracture. We run the complex case with stimulated secondary fracture network, and compare the result with the single fracture configuration. The intrinsic matrix permeability is 1.0e-19 m^2, and the half-length for the single hydraulic fracture is 50m. The mesh configurations of the two cases are shown in **Fig. 3.18**. The pressure profiles at 50/200 day for the complex case are shown in **Fig. 3.19**. The log-log plot of the gas rates is shown in **Fig. 3.20**, and we also generate the plot of inverse gas rate vs. $\sqrt{t}$ based on the theory for linear flow analysis in **Fig. 3.21**. As can be seen from the results, the fracture network that involves secondary fractures greatly improves the gas rate, and creates a more complicated flow pattern. From the plot of $1/q_g$ vs. sqrt(t), we could observe a sharp transition in the curve slope, due to the rapid depletion of the small drainage area within the secondary fracture network. In addition, an elliptical flow regime around the fracture network is observed in the pressure profile, which results in a gradual slope transition to the formation linear flow in terms of the base hydraulic fracture.

We also establish three cases for the fracture network with complex pattern. The mesh configurations for the three cases are shown in **Fig. 3.22**. The plot of inverse gas rate versus sqrt(t) for the base case (contains only a single hydraulic fracture) and the three complex cases is shown in **Fig. 3.23**.

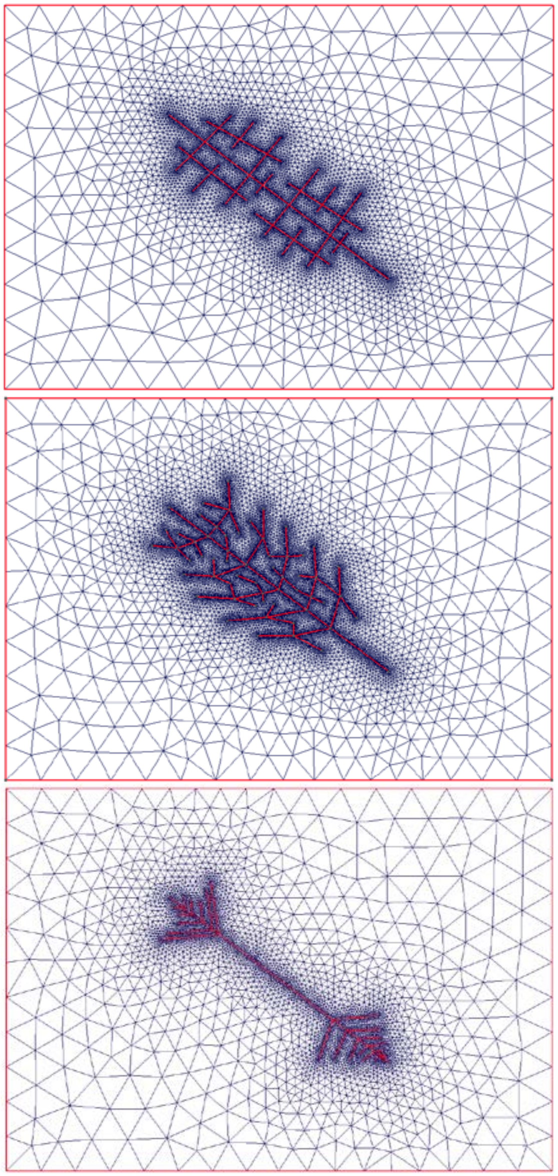

Figure 3.22: Mesh configurations of the three cases.

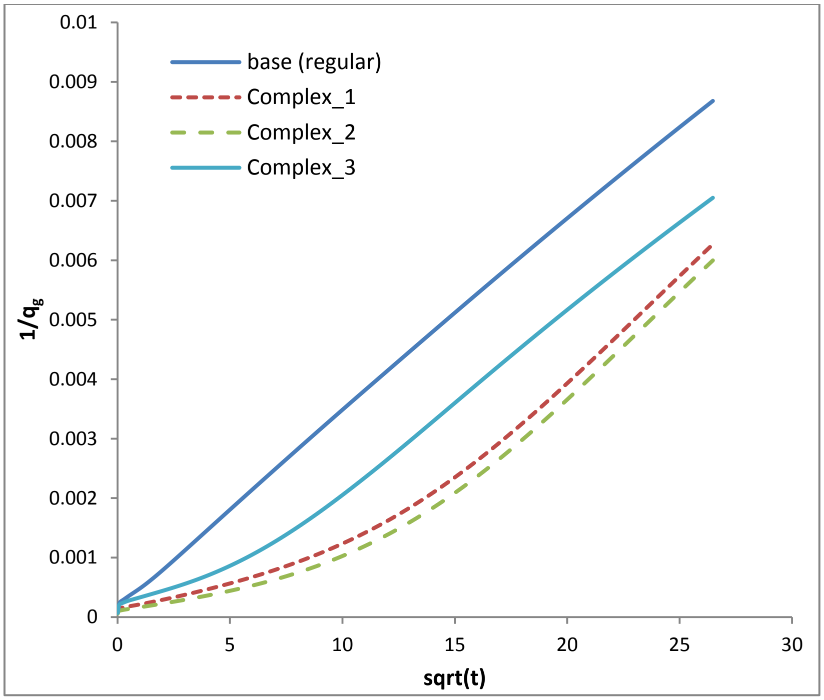

Figure 3.23: The plot of inverse gas rate vs. $\sqrt{t}$ for the base case and the three complex cases.

3.2.7 Effects on the Interpretation of Rate Transient Data

Early time production data from multi-fractured horizontal wells typically exhibit linear flow for an extended period and are analyzed using a variety of specialized plots. In this section we restrict ourselves to RTA analysis using linear superposition time

$$t_{sup} = \sum_{i=1}^{n} \frac{q_i - q_{i-1}}{q_n} \sqrt{t_n - t_{i-i}}, \tag{3.15}$$

where t_i is the time at which the rate q_i is observed, and we consider the impact of fracture geometry on the analysis results. Since we are primarily interested in the period prior to fracture interference, it suffices to consider a single (complex) fracture and its drainage region. We assume that this region contains only gas (Methane) with matrix properties as summarized in Table 3.3 (These properties are typical of horizontal well in the Cana Woodford Shale reservoir).

Table 3.3: Model parameters.

Parameter	Value	Unit
Reservoir dimensions (x,y,z)	100, 500, 201	ft
Initial reservoir pressure	8820	psia
Temperature	207	F
Matrix porosity	0.08	
Fracture permeability	1	d
Fracture half-length	200	ft
Producer BHP	2000	psia
Production time	400	day

As is typical for field observations, production data are measured on a daily basis, so any rate transient features whose duration is less than one day are not observable. For this part of the study, we consider four fracture geometries, all with the same underlying fracture half length); geometries for the complex fracture cases are depicted in **Fig. 3.24**.

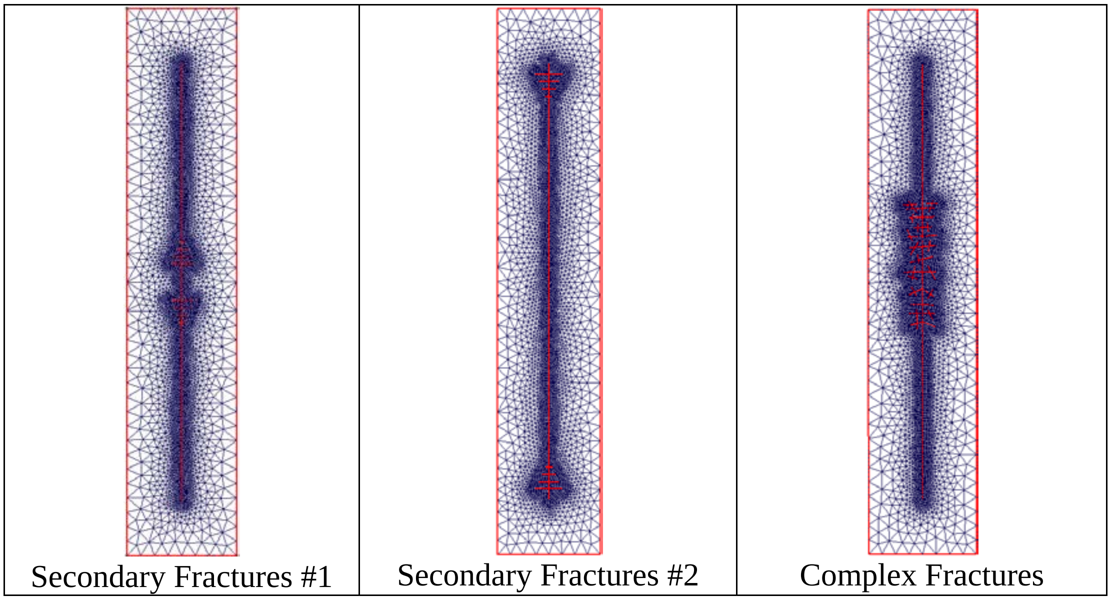
Secondary Fractures #1
Secondary Fractures #2
Complex Fractures

Figure 3.24: Complex fracture geometries investigated for RTA Analysis.

We produced each of the systems at constant bottom-hole flowing pressure for 400 days, and plot the resulting rate-normalized pseudopressure drops versus linear superposition time as shown in **Fig. 3.25**. All of the systems yielded straight lines at late times with slopes within 3% of the base case slope, but with negative intercepts that increased in magnitude as the fracture complexity increased. We computed estimates of fracture half length x_f from the slopes (m) of the superposition plot using

$$\sqrt{k}x_f = \frac{200.8T}{mh}\sqrt{\frac{1}{\varphi\mu_i c_{ti}}} \tag{3.16}$$

and the input value of permeability (10 nd); these values are shown in Table 3.4. As expected, these values are high due to the variation in gas compressibility-viscosity product. We apply the drawdown correction suggested by Ibrahim and Wattenbarger (2006)

$$f_{CP} = 1 - 0.0852D_D - 0.0857D_D^2 \tag{3.17}$$

where,

$$D_D = \frac{m(p_i) - m(p_{wf})}{m(p_i)} \tag{3.18}$$

and obtained agreement within 5% of the input data (200 ft).

Table 3.4: Input and interpreted values.

Case	Slope	x_f, ft	Correction, f_{CP}	x_f, ft (corrected)
Base	2219	238	0.85	203
Secondary Frac. # 1	2196	240	0.85	205
Secondary Frac. # 2	2147	246	0.85	209
Complex	2147	246	0.85	209

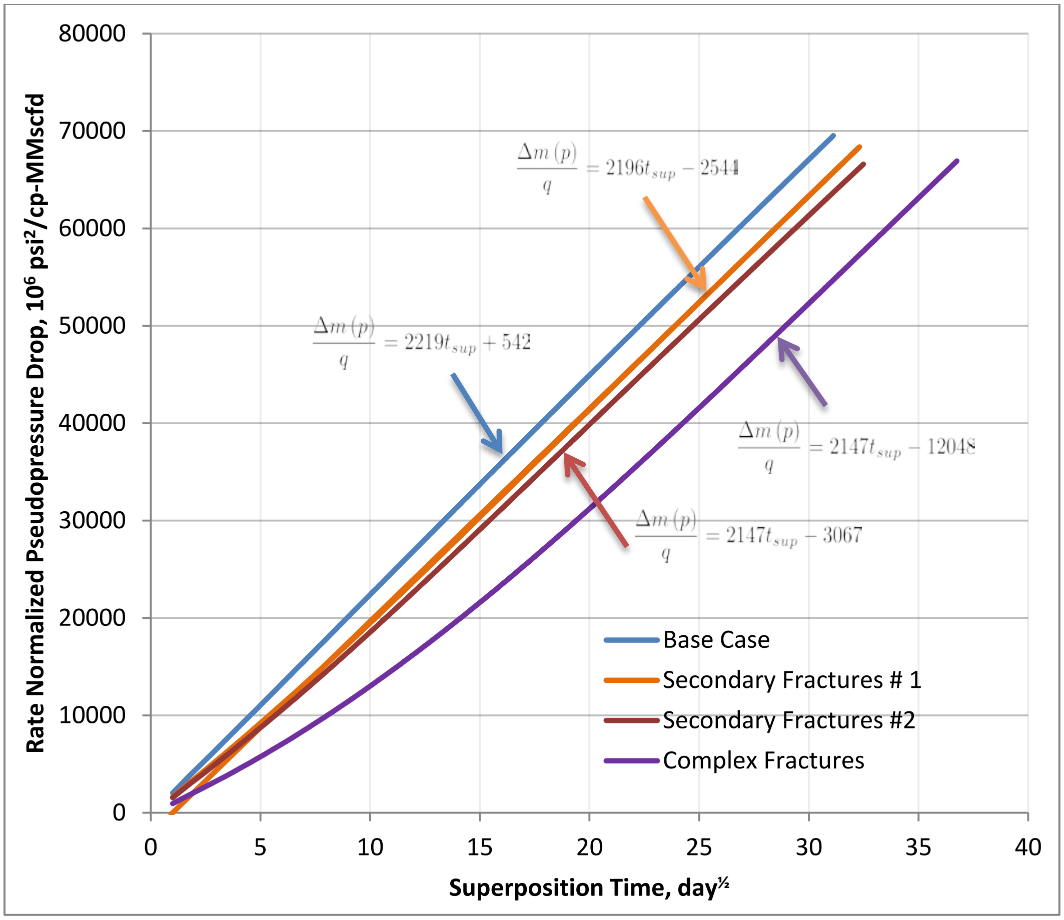

Figure 3.25: Superposition Time plots.

These results suggest that increasing fracture complexity does not affect the late time estimate of matrix flow capacity, $\sqrt{k}x_f$. Complex fractures offer a high initial open area to flow from matrix to fracture system, and this results in a negative intercept, but this initial effect gradually fades as flow in the matrix becomes directed linearly to the base fracture half length.

CHAPTER 4

CONCLUSIONS

In this work, we develop a generic simulation platform which allows investigators to rapidly implement and experiment with a wide array of alternate physical and constitutive models. The simulation platform is designed to incorporate the spectrum of known physics inherent in unconventional gas reservoirs, such as the non-Darcy effect covering various flow regimes, multi-phase behavior, adsorption/desorption, high-velocity turbulent flow, as well as the rock un-consolidation of natural fractures network. We also implement a compositional module in the simulation platform, for simulating the advanced processes such as injecting CO_2 into fractured shale gas reservoirs to simultaneously enhance gas recovery while sequester carbon.

We develop two types of hybrid technique that integrate DFM with continuum-type approaches for the accurate and efficient modeling of the multi-scaled fracture system in stimulated unconventional formations.

The first hybrid model couples EDFM with MINC (EDFM-MINC) in order to simulate the SRV for hydraulically fractured tight- and shale plays when detailed fracture characterization data for the small-scale fractures is not available. The model is validated by comparison to the LS-LR reference solutions. The results show that the model could provide better computational efficiency relative to LS-LR while adequately capturing the sharp local transients in the ultra-tight matrix. Moreover, flexibility could be obtained to model the complex geometry of hydraulic fractures.

The second class of hybrid model proposed integrates the unstructured DFM with the continuum-type approaches (UDFM-MINC). Optimized local grid refinement (LGR) is employed to accurately handle the transient flow regime around primary fractures. An upscaling technique is also implemented within the hybrid fracture model in order to capture the complex distribution of small-scale/natural fractures using a DK model. The potential gradient associated with the fracture and matrix continua could be resolved using the refined gridding around primary fractures. We validate the hybrid model and the associated upscaling procedure by comparison to a fine-scale DFM model where all fractures are discretized explicitly. The results indicate that the hybrid model provides accurate solutions for both early transient and long-term production periods.

Phase equilibrium calculations for CO_2-water/brine system are important during the CO_2-EGR process because aqueous phase are generally present in shale gas reservoirs. Therefore a modified EOS is implemented in the phase package of the developed simulator to accurately model the mutual solubilities of CO_2/hydrocarbon-brine mixtures. In addition, we consider both effects of pore proximity and capillary pressure for the developed compositional model.

We conduct comprehensive modeling studies towards understanding the key reservoir and fracture properties that affect the production performance, and investigating the feasibility of CO_2 injection for carbon sequestration and enhanced methane recovery in shale gas reservoirs. We could obtain following conclusions from the simulation results in chapter 3:

1. Capillary pressure reduces the water evaporation, and the critical properties shift caused by pore confinement effect could increase the water mole fraction in gas phase;

2. CO_2 injection into shale gas reservoirs appears to be a technically feasible method for CO_2 storage and methane recovery enhancement.

In addition, we implement a lower-dimensional DFM model based on unstructured gridding for handling the non-ideal, non-planar fracture geometries of hydraulic fracture in chapter 4. Mimetic finite difference (MFD) method is applied for discretizing the lower-dimensional DFM model.

We examine the effects of the complex fracture pattern with the non-orthogonal, non-planar and inclined fracture geometries on the production profile of multiple-fractured horizontal well in unconventional gas reservoir. Rate transient analysis (RTA) is performed using the theory of linear flow analysis for several simulation cases. We could obtain following conclusions from the simulation results:

1. The gas rates of the cases with non-orthogonal fracture geometry gradually deviate from the orthogonal case after the occurrence of fracture interference, and the case with smaller fracture angularity exhibits fracture interference earlier. The non-orthogonal fracture systems also have lower production than the orthogonal case with the same fracture half-length;
2. The inclined fracture systems have higher production than the vertical fracture case, because the reservoir volume connecting to the top and bottom boundaries of the fracture plane for the inclined fracture is larger than the vertical fracture;
3. The fracture network that involves secondary fractures greatly improves the gas rate, and creates a more complicated flow pattern. From the plot of $1/q_g$ vs. sqrt(t) for the complex case, a sharp transition in the curve slope is observed, due to the rapid depletion of the small drainage area within the secondary fracture network. An elliptical flow

regime around the fracture network is also observed in the pressure profile, which results in a gradual slope transition to the formation linear flow in terms of the base hydraulic fracture;

4. The RTA results suggest that increasing fracture complexity does not affect the late time estimate of matrix flow capacity, $\sqrt{k}x_f$. Complex fractures offer a high initial open area to flow from matrix to fracture system, and this results in a negative intercept, but this initial effect gradually fades as flow in the matrix becomes directed linearly to the base fracture half length.

BIBLIOGRAPHY

Aavatsmark, I., An Introduction to Multipoint Flux Approximations for Quadrilateral Grids. *Computational Geosciences*, 6(3-4):405-432, 2002. ISSN 1420-0597.

Alpak, F.O., A Mimetic Finite Volume Discretization Method for Reservoir Simulation. *SPEJ*. June 2010.

Azizi, N., Behbahani, R., Isazadeh, M.A., An Efficient Correlation for Calculating Compressibility Factor of Natural Gases, Journal of Natural Gas Chemistry. 19: 642-645, 2010.

Ahmed Elfeel, M. and Geiger, S. Static and Dynamic Assessment of DFN Permeability Upscaling. SPE 154369 presented at the EAGE Annual Conference & Exhibition incorporating SPE Europec held in Copenhagen, Denmark, 4-7 June 2012.

Bogdanov, I.I., Mourzenko, V.V., Thovert, J.-F., and Adler, P.M. 2003. Effective Permeability of Fractured Porous Media in Steady State Flow. *Water Resour. Res.* 39 (1): 1023-1038. DOI: 10.1029/2001WR000756.

Brezzi, F., Lipnikov, K., Simoncini, V., A family of mimetic finite difference methods on polygonal and polyhedral meshes. Math. Models Methods Appl. Sci. 15, 1533-1553 (2005). Doi:10.1142/S0218202505000832

Cipolla, C.L., Warpinski, N.R., Mayerhofer, M.J., Lolon, E.P., The Relationship Between Fracture Complexity, Reservoir Properties, and Fracture Treatment Design, SPE 115769 presented at the SPE ATCE, Denver, Colorado, 2009.

Cipolla, C.L., Lolon, E.P., Erdle, J.C., Rubin, B., Reservoir Modeling in Shale-Gas Reservoirs, *Reservoir Eval.& Eng.*, August 2010.

Cipolla, C.L., Fitzpatrick, T., Williams, M.J., Ganguly, U.K., Seismic-to-Simulation for Unconventional Reservoir Development, SPE 146876 presented at the SPE Reservoir Characterisation and Simulation Conference and Exhibition, Abu Dhabi, UAE, October 2011.

Chen, C., Raghavan, R., On the Liquid-Flow Analog to Evaluate Gas Wells Producing in Shales, *SPE Reservoir Evaluation & Engineering*, May 2013.

Dershowitz, B., Lapointe P., Eiben, T., Wei, L.L., Integration of Discrete Fracture Network Methods with Conventional Simulator Approaches, *SPE Reservoir Eval.& Eng.*, April 2000.

Ding, Y., Basquet, R., Bourbiaux, B., Upscaling Fracture Networks for Simulation of Horizontal Wells Using a Dual-Porosity Reservoir Simulator, *SPE Reservoir Eval. & Eng.*, October 2006.

Florence, F.A., Rushing, J.A., Newsham, K.E., Blasingame, T.A. Improved Permeability Prediction Relations for Low Permeability Sands, SPE 107954 presented at the 2007 SPE Rocky Mountain Oil and Gas Technology Symposium, Denver, Colorado, USA, April 2007.

Freeman, C.M., Moridis, G.J., Ilk, D., Blasingame, T.A., A Numerical Study of Transport and Storage Effects for Tight Gas and Shale Gas Reservoir Systems, SPE 131583, SPE International Oil & Gas Conference and Exhibition held in Beijing, China, June 2010.

Freeman, C.M., Moridis, G., Ilk, D., Blasingame, T.A., A Numerical Study of performance for tight gas and shale gas reservoir systems. *Journal of Petroleum Science and Engineering*. 2013.

Farah, N., Ding, D.Y., Wu, Y.S., Khrouf, A.M., Simulation of Fracturing Water Invasion and its Impact on Gas Production in Shale-gas Reservoirs, European Conference on the Mathematics of Oil Recovery, Catania, Sicily, Italy, September 2014.

Gong, B., Karimi-Fard, M., Durlofsky, L.J. 2008. Upscaling Discrete Fracture Characterizations to Dual-Porosity, Dual-Permeability Models for Efficient Simulation of Flow With Strong Gravitational Effects. *SPEJ*.

Geiger, S., Matthai, S., Niessner, J., Helmig, R. Black-Oil Simulations for Three-Component, Three-Phase Flow in Fractured Porous Media. *SPEJ.* June 2009.

Geiger, S., Dentz, M., Neuweiler, I., A Novel Multirate Dual-Porosity Model for Improved Simulation of Fractured and Multiporosity Reservoirs. *SPEJ*. August 2013.

Ho, C.K., Webb, S.W., Gas Transport in Porous Media (2006), Springer, Netherlands.

Houze, O.P., Tauzin, E., Artus, V. et al. 2010. The Analysis of Dynamic Data in Shale Gas Reservoirs---Part 1. Company report, Kappa Engineering, Houston, Texas.

Hoteit, H. and Firrozabadi, A. 2005. Multicomponent Fluid Flow by Discontinuous Galerkin and Mixed Methods in Unfractured and Fractured Media. Water Resour. Res. 41: W11412. DOI: 10.1029/2005WR004339.

Hoteit, H., Firoozabadi, A., An Efficient Numerical Model for Incompressible Two-phase Flow in Fractured Media, 2008. *Advances in Water Resources*. 31:891-905.

Holm, R., Kaufmann, R., Heimsund, B.-O., Oian, E., Espedal, M.S. Meshing of domains with complex internal geometries. *Numerical Linear Algebra with Applications*. 2006. 13:717-731.

Hajibeygi, H., Karvounis, D., Jenny, P., A hierarchical Fracture Model for the Iterative Multiscale Finite Volume Method, *Journal of Computational Physics*, 2011.

Hinkley, R., Gu, Z.Q., Wong, T., Camilleri, D. Multi-Porosity Simulation of Unconventional Reservoirs. SPE 167146 presented at the SPE Unconventional Resources Conference-Canada held in Calgary, Alberta, Canada, November 2013.

Hui, M.-H., Mallison, B., Heidary-Fyrozjaee, M., Narr, W., The Upscaling of Discrete Fracture Models for Faster, Coarse-Scale Simulations of IOR and EOR Processes for Fractured Reservoirs. SPE 166075 presented at the SPE Annual Technical Conference and Exhibition held in New Orleans, Louisiana, USA, 30 September-2 October 2013.

Ibrahim, M. and Wattenbarger, R.A. Rate Dependence of Transient Liner Flow in Gas Wells *J. Cdn. Pet. Tech.* (2006) **45** (10) 18-20.

Juanes, R., Samper, J. and Molinero, J. 2002. A General and Efficient Formulation of Fractures and Boundary Conditions in the Finite Element Method. *Int. J. Numer. Methods Eng.* 54 (12): 1751-1774. DOI:10.1002/nme.491.

Javadpour, F., Fisher, D., Unsworth, M., Nanoscale Gas Flow in Shale Gas Sediments, *Journal of Canadian Petroleum Tech.*, 2007.

Jiang, J.M., Younis, R.M., A Multi-continuum Compositional Model for CO_2-EGR Process in Stimulated Fractured Shale Gas Reservoirs, European Conference on the Mathematics of Oil Recovery, Catania, Sicily, Italy, September 2014.

Jiang, J.M., Younis, R.M., A Generic Physics-based Numerical Platform with Hybrid Fracture Modelling Techniques for Simulating Unconventional Gas Reservoirs. SPE 173318 presented at the SPE Reservoir Simulation Symposium held in Houston, Texas, USA, 23-25 February 2015.

Kazemi, H., Merrill, L.S., Porterfield, K.L., Zeman, P.R., Numerical Simulation of Water-Oil Flow in Naturally Fractured Reservoirs, *SPEJ*, December 1976.

Kim, J.-G., Deo, M.D. Finite-element, discrete-fracture model for multiphase flow in porous media. *AIChE Journal*. June 2000, Vol. 46, No.6.

Karniadakis, G.E., Beskok, A., Microflows: Fundamentals and Simulation. Springer, Berlin (2001).

Karimi-fard, M., Firoozabadi, A., Numerical Simulation of Water Injection in Fractured Media Using the Discrete-Fracture Model and the Galerkin Method, *SPE Journal*, 2003.

Karimi-fard, M., Durlofsky, L.J., Aziz, K., An Efficient Discrete-Fracture Model Applicable for General Purpose Reservoir Simulators, *SPE Journal*, 2004.

Karimi-Fard, M., Gong, B., Durlofsky, L.J. 2006. Generation of coarse-scale continuum flow models from detailed fracture characterizations. *Water Resources Research*. W10423, doi:10.1029/2006WR005015.

Lee, A.L., Gonzalez, M.H., Eakin, B.E., The Viscosity of Natural Gases, *JPT*, Trans., AMIE, 37, August 1966.

Lee, S.H., Lough, M.F., Jensen, C.L., Hierarchical Modeling of Flow in Naturally Fractured Formations with Multiple Length Scales, *Water Resources Research*, 2001.

Li, L., Lee, S.H., Efficient Field-Scale Simulation of Black Oil in a Naturally Fractured Reservoir Through Discrete Fracture Networks and Homogenized Media, *SPEREE*, 2008.

Lie, K.A., Krogstad, S., Ligaarden, I.S., Natvig, J.R., Nilsen, H.M., Skaflestad, B., Open-source Matlab Implementation of Consistent Discretisations on Complex Grids. *Computational Geosciences*, 16(2):297-322, 2012. ISSN 1420-0597.

Mayerhofer, M.J., Lolon, E.P., Youngblood, J.E., Heinze, J.R., Integration of Microseismic Fracture Mapping Results with Numerical Fracture Network Production Modeling in the Barnett Shale, SPE 102103 presented at the SPE Annual Technical Conference and Exhibition, San Antonio, Texas, USA, September 2006.

Moridis, G.J., Blasingame, T.A., Freeman, C.M., Analysis of Mechanisms of Flow in Fractured Tight-Gas and Shale-Gas Reservoirs, SPE 139250, SPE Latin American & Caribbean Petroleum Engineering Conference, Lima, Peru, December 2010.

Moridis, G.J., Freeman, C.M., The RealGas and RealGasH2O options of the TOUGH+ Code for the Simulation of Coupled Fluid and Heat Flow in Tight/Shale Gas Systems, *Computers & Geosciences*, September, 2013.

Monteagudo, J.E.P. and Firoozabadi, A. 2004. Control-Volume Method for Numerical Simulation of Two-Phase Immiscible Flow in Two- and Three-Dimensional Discrete-Fractured Media. Water Resour. Res. 40:W07405. DOI: 10.1029/2003WR002996.

Matthai, S., Menzentsev, A., Belayneh, M., Control-Volume Finite-Element Two Phase Flow Experiments with Fractured Rock Represented by Unstructured 3D Hybrid

Meshes, SPE 93341, SPE Reservoir Simulation Symposium, Houston, TX, February 2005.

Moinfar, A., Narr, W., Hui, R., Mallison, B., Lee, S.H., Comparison of Discrete-Fracture and Dual-Permeability Models for Multiphase Flow in Naturally Fractured Reservoirs, SPE 142295, SPE Reservoir Simulation Symposium, The Woodlands, TX, February 2011.

Moinfar, A., Varavei, A., Sepehrnoori, K., Johns, R.T., Development of a Novel and Computationally-Efficient Discrete-Fracture Model to Study IOR Processes in Naturally Fractured Reservoirs, SPE 154246, Symposium on Improved Oil Recovery, Tulsa, OK, April 2012.

Moinfar, A., Varavei, A., Sepehrnoori, K., Johns, R.T., Development of a Coupled Dual Continuum and Discrete Fracture Model for the Simulation of Unconventional Reservoirs, SPE 163647, SPE Reservoir Simulation Symposium, The Woodlands, TX, February 2013.

Moog, G.J., Advanced Discretization Methods for Flow Simulation Using Unstructured Grids, PhD thesis, Stanford University, 2013.

Maier, C., Geiger, S., Combining Unstructured Grids, Discrete Fracture Representation and Dual-Porosity Models for Improved Simulation of Naturally Fractured Reservoirs. SPE 166049 presented at the SPE Reservoir Characterisation and Simulation Conference and Exhibition held in Abu Dhabi, UAE, 16-18 September 2013.

Ozkan, E., Raghavan, R., New Solutions for Well-Test-Analysis Problems: Part 1---Analytical Considerations, *SPE Formation Evaluation*, September 1991.

Ozkan, E., Raghavan, R., New Solutions for Well-Test-Analysis Problems: Part 2---Computational Considerations and Applications, *SPE Formation Evaluation*, September 1991.

Olorode, O.M., Freeman, C.M., Moridis, G.J., Blasingame, T.A., High-Resolution Numerical Modeling of Complex and Irregular Fracture Patterns in Shale-Gas Reservoirs and Tight Gas Reservoirs, *SPE Reservoir Evaluation & Engineering*, November 2013.

Persson, P.O., Strang, G. A Simple Mesh Generator in Matlab. *SIAM Review* 2004. 46(2):329-345.

Pruess, K. and T.N. Narasimhan, A Practical Method for Modeling Fluid and Heat Flow in Fractured Porous Media, *Soc. Pet. Eng. J.*, 1985.

Persson, P.O., Strang, G. A Simple Mesh Generator in Matlab. *SIAM Review* 2004. 46(2):329-345.

Rubin, B. Accurate Simulation of Non-Darcy Flow in Stimulated Fractured Shale Reservoir. Paper SPE 132093 presented at the SPE Western Regional Meeting, Anaheim, CA, USA, 27-29, May 2010.

Reichenberger, V., Jakobs, H., Bastian, P., Helmig, R. A mixed-dimensional finite volume method for two-phase flow in fractured porous media. Advances in Water Resources. 2006.

Singh, G. Mimetic Finite Difference Method on GPU. Master thesis, Norwegian University of Science and Technology, July 2010.

Sandve, T.H., Berre, I., Nordbotten, J.M., An Efficient Multi-point Flux Approximation Method for Discrete Fracture-Matrix Simulations, *Journal of Computational Physics*, January 2012.

Tecklenburg, J., Neuweiler, I., Dentz, M., Carrera, J., Geiger, S., Abramowski, C., Silva, O. A non-local two-phase flow model for immiscible displacement in highly heterogeneous porous media and its parametrization. *Advances in Water Resources*. June 2013.

Vitel, S., Souche, L., Unstructured Upgridding and Transmissibility Upscaling for Preferential Flow Paths in 3D Fractured Reservoirs, SPE 106483 presented at the 2007 SPE Reservoir Simulation Symposium held in Houston, Texas, USA.

Wu, Y.S., Pruess, K., A Multiple-Porosity Method for Simulation of Naturally Fractured Petroleum Reservoirs, *SPE Reservoir Engineering*, February 1988.

Wu, Y.S., Fakcharoenphol, P., A Unified Mathematical Model for Unconventional Reservoir Simulation, SPE 142884 presented at the SPE EUROPEC/EAGE Annual Conference and Exhibition held in Vienna, Austria, May 2011.

Wu, Y.S., Li, J.F., Ding D., Wang, C., Di, Y., A Generalized Framework Model for Simulation of Gas Production in Unconventional Gas Reservoirs, SPE 163609 presented at the SPE Reservoir Simulation Symposium held in The Woodlands, Texas, February 2013.

Weng, X.W., Kresse, O., Chuprakov, D., Cohen, C., Prioul, R., Ganguly, U. Applying complex fracture model and integrated workflow in unconventional reservoirs. Journal of Petroleum Science and Engineering. October 2014.

Warpinski, N.R., Mayerhofer, M.J., Vincent, M.C., Cipolla, C.L., Lolon, E.P. Stimulating Unconventional Reservoirs: Maximizing Network Growth While Optimizing Fracture Conductivity? SPE 114173 presented at the SPE Unconventional Reservoirs Conference, Keystone, Colorado, USA, February 2008.

Xu, G.S., Wong, S.-W. 2013. Interaction of multiple non-planar hydraulic fractures in horizontal wells. International Petroleum Technology Conference, 26-28 March, Beijing, China. IPTC 17043.

Wilson, K.C., Durlofsky, L.J., Optimization of shale gas field development using direct search techniques and reduced-physics models. Journal of Petroleum Science and Engineering. May 2013.

Younis, R.M., Aziz, K., Parallel Automatically Differentiable Data-Types for Next-Generation Simulator Development, SPE 106493, SPE Reservoir Simulation Symposium held in Houston, Texas, February 2007.

Younis, R.M., Modern Advances in Software and Solution Algorithms for Reservoir Simulation, PhD thesis, Stanford University, 2011.

Younis, R.M., Tchelepi, H.A., Lazy K-Way Linear Combination Kernels for Efficient Runtime Sparse Jacobian Matrix Evaluations in C++, *Advances in Algorithmic Differentiation*, Springer, 2012.

Zimmerman, R.W., Hadgu, T., Bodvarsson, G.S., A new lumped-parameter model for flow in unsaturated dual-porosity media. *Advances in Water Resources*, Vol. 19, No. 5, pp 317-327, 1996.